Journal Pre-proof

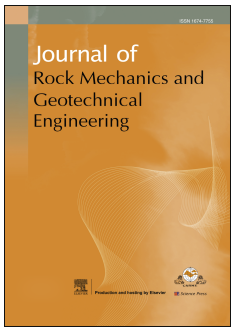

Design optimization of quasi-rectangular tunnels based on hyperstatic reaction method and ensemble learning

Tai-Tien Nguyen, Ba-Trung Cao, Van-Vi Pham, Hoang-Giang Bui, Ngoc-Anh Do

PII: S1674-7755(24)00549-3

DOI: https://doi.org/10.1016/j.jrmge.2024.10.020

Reference: JRMGE 1837

To appear in: *Journal of Rock Mechanics and Geotechnical Engineering*

Received Date: 10 June 2024

Revised Date: 14 September 2024

Accepted Date: 21 October 2024

Please cite this article as: Nguyen T-T, Cao B-T, Pham V-V, Bui H-G, Do N-A, Design optimization of quasi-rectangular tunnels based on hyperstatic reaction method and ensemble learning, *Journal of Rock Mechanics and Geotechnical Engineering*, https://doi.org/10.1016/j.jrmge.2024.10.020.

Full Length Article

Design optimization of quasi-rectangular tunnels based on hyperstatic reaction method and ensemble learning

Tai-Tien Nguyen[a, b], Ba-Trung Cao[c, *], Van-Vi Pham[a], Hoang-Giang Bui[d], Ngoc-Anh Do[a, b]

[a] Sustainable Development in Underground Engineering Research Team, Hanoi University of Mining and Geology, Hanoi, Vietnam

[b] Department of Underground and Mining Construction, Faculty of Civil Engineering, Hanoi University of Mining and Geology, Hanoi, Vietnam

[c] Institute for Structural Mechanics, Ruhr University Bochum, Bochum, Germany

[d] Institute of Material Systems Modeling, Helmholtz-Zentrum Hereon, Geesthacht, Germany

[*]Corresponding author. E-mail address: ba.cao@rub.de (Ba-Trung Cao)

Abstract: The quasi-rectangular tunnel represents a novel cross-section design, intended to supersede the traditional circular and rectangular tunnel formats. Due to the limited capacity of the tunnel vault to withstand vertical loads, an interior column is often installed at the center to enhance its load-bearing capacity. This study aims to develop a hyperstatic reaction method (HRM) for the analysis of deformation and structural integrity in this specific tunnel type. The computational model is validated through comparison with the corresponding finite element method (FEM) analysis. Following comprehensive validation, an ensemble machine learning (ML) model is proposed, using numerical benchmark data, to facilitate real-time design and optimization. Subsequently, three widely used ensemble models, i.e. random forest (RF), gradient boosting decision tree (GBDT), and extreme gradient boosting (XGBoost) are compared to identify the most efficient ML model for replacing the HRM model in the design optimization process. The performance metrics, such as the coefficient of determination R^2 of about 0.999 and the mean absolute percentage error (MAPE) of about 1%, indicate that XGBoost outperforms the others, exhibiting excellent agreement with the HRM analysis. Additionally, the model demonstrates high computational efficiency, with prediction times measured in seconds. Finally, the HRM-XGBoost model is integrated with the well-known particle swarm optimization (PSO) for the real-time design optimization of quasi-rectangular tunnels, both with and without the interior column. A feature importance assessment is conducted to evaluate the sensitivity of design input features, enabling the selection of the most critical features for the optimization task.

Keywords: Hyperstatic reaction method (HRM), Quasi-rectangular tunnel, Tunnel lining, Numerical analysis, Real-time design, Optimization, Extreme gradient boosting (XGBoost), Shapley additive explanations (SHAP)

1. Introduction

The quasi-rectangular tunnel has recently been proposed as a new tunnel cross-sectional design to address the inherent limitations of conventional circular and rectangular tunnels. The advantages of this tunnel cross-sectional design include higher space utilization and the elimination of concentrated stress induced at corners, which are inherent weaknesses in circular and rectangular tunnels (Huang et al., 2018; Do et al., 2020; Dang et al., 2021; Liu et al., 2024). Liu et al. (2018a) demonstrated that a quasi-rectangular tunnel can save approximately 20% more space than a traditional circular tunnel. However, one of the limitations of quasi-rectangular tunnels is the restricted capacity of the tunnel vault to resist vertical loads, due to the flatness of this section caused by the large radius. To address this issue, an interior column is frequently incorporated into the design at the tunnel center to enhance the load-bearing capacity of the tunnel lining. Furthermore, the column serves as a structural element to separate the two transportation lanes within the tunnel.

Recently, the behavior of quasi-rectangular tunnel support structures without an interior column has been studied using various methods, including experiments (Huang et al., 2018; Zhang et al., 2019, 2022a, b; Gong et al., 2024), and numerical analysis (Huang et al., 2018; Zhu et al., 2018; Do et al., 2020; Tien et al., 2020; Liu et al., 2024). The findings of these studies indicate that the dimensions, shape, buried depth, joint properties, and external loading distribution of the tunnel significantly influence its behavior.

The impact of the interior column on the behavior of quasi-rectangular tunnels has also been explored through experimental and numerical methods (Liu et al., 2018a, c; Zhang et al., 2020, 2022a; Zhang, 2021; Nguyen and Do, 2024). When an interior column is installed, the distribution of bending moment along the tunnel periphery changes, sometimes contrasting with those observed in a quasi-rectangular tunnel without a column. Specifically, negative bending moments are predicted at the tunnel vault and bottom, while positive bending moments are observed at the tunnel waist, indicating that the tensile parts of the tunnel lining become compressed (Zhao et al., 2021). Furthermore, the presence of the interior column alters the normal and shear forces within the lining (Liu et al., 2018b, c; Zhao et al., 2021).

Most studies have focused on the effect of segment joints and external loading schemes on the

behavior of tunnel linings. Using an analytical solution, Yu and Chen (2021) conducted a parametric study to investigate the impact of the interior wall's thickness on quasi-rectangular tunnel lining behavior. A constant tunnel lining thickness of 0.45 m was maintained, while the ratio between the interior wall thickness and that of the tunnel lining varied from 0.5 to 4. The results highlighted a significant influence of this thickness ratio on the tangential stress in the tunnel lining, particularly in the area near the connection between the interior column and the lining.

The study of quasi-rectangular tunnels has recently attracted considerable interest from researchers, both those with and without interior column cases, using various approaches. Among these studies, Do et al. (2020) and Du et al. (2022) developed the hyperstatic reaction method (HRM) to conduct a comprehensive numerical investigation of quasi-rectangular tunnels without interior columns. This method, which is based on the finite element method (FEM) and was introduced by Oreste (2007) and other researchers (Do et al., 2014; Du et al., 2018, 2020a; Tien et al., 2020; Nguyen et al., 2022; Pham et al., 2021, 2022), offers several advantages, including efficiency due to small discretization size and the use of nodal elastic springs. The HRM applies to various tunnel types, accounting for different shapes, ground conditions with multi-layers of varying properties, and asymmetry in external ground loading. This study aims to extend the HRM method to quasi-rectangular tunnels with an interior column at the tunnel center. The method has been validated through comparison with FEM analysis using Plaxis2D software (Plaxis, 2019) in several quasi-rectangular tunnel cross-sections.

Generally, the HRM model can be combined with optimization algorithms for the design optimization of a quasi-rectangular tunnel. However, in scenarios where a large number of design alternatives are required to identify the optimum design variant, it is essential to conduct repeated numerical predictions of the tunnel response, with the results delivered in real-time. To accelerate the design optimization process and enable real-time prediction, it is necessary to substitute numerical simulations with computationally inexpensive surrogate models. For example, surrogate models can be integrated with particle swarm optimization (PSO) (Eberhart and Shi, 2001) to support decision-making in tunneling applications, such as the optimization of operational parameters during tunnel construction (Li et al., 2023a; Liu et al., 2023) or the optimization of anchoring parameters in rock tunnels (Li et al., 2021a). Theoretically, various methods can be employed to construct surrogate models for tunneling applications, including model order reduction techniques, including proper orthogonal decomposition (Cao et al., 2016; Zendaki et al., 2024), traditional machine learning (ML) models such as feed-forward neural networks (Cao et al., 2020; Zhao et al., 2024), recurrent neural networks (Freitag et al., 2018;

Cao et al., 2022), support vector machines (Huang et al., 2022; Li et al., 2024), deep learning (Tang and Na, 2021; Elbaz et al., 2022), and physics-informed machine learning (Xu et al., 2023, 2024), and ensemble learning with tree-based algorithms such as random forest (RF) (Zhang et al., 2021), gradient boosting decision tree (GBDT) (Bui et al., 2023), and extreme gradient boosting (XGBoost) (Li et al., 2021b). Comparative studies have demonstrated that ensemble learning is the most accurate and efficient model for small to medium datasets (Li et al., 2021b; Zhang et al., 2021). Moreover, a tree-based ensemble can identify the sensitivity of features on prediction results, which is beneficial for evaluating the importance of model inputs. To the best of the authors' knowledge, no comparable studies have been conducted concerning the quasi-rectangular tunnel. Therefore, in this study, three widely used tree-based ensemble ML models are utilized as surrogate models for the HRM simulation model to perform feature importance analysis. A comparative study is conducted to determine the most efficient ML model, which is then combined with the PSO to achieve real-time design optimization of quasi-rectangular tunnels.

This paper is structured as follows. After the Introduction, Section 2 presents an improved HRM model for the case of a quasi-rectangular tunnel with an interior column, validated by comparisons with FEM results. Furthermore, a parametric study is conducted using the developed HRM model, considering various input parameters, including tunnel depth, lining thickness, Young's modulus of the soil, and lateral earth pressure coefficient. The data obtained in Section 2 will be thoroughly analyzed in Section 3, where ML algorithms are implemented and tested for predicting maximum and minimum stresses in the lining. Section 4 is dedicated to the analysis of the importance of input features related to stress outputs. In Section 5, the ML models, together with the PSO algorithm, are utilized to determine the optimal values for the lining thickness and the thickness of the interior column. Finally, conclusions and suggestions for future work are presented in Section 6.

2. Development of the HRM model for a quasi-rectangular tunnel with an interior column

2.1. Development of the HRM

The HRM is a numerical technique built upon the FEM, in which the structure is discretized using beam elements. The interaction between the structure and the surrounding ground is characterized by Winkler springs at the nodal points. The relationship between the displacement and the applied load for the entire structure is expressed through the following equation:

$$\boldsymbol{K}\boldsymbol{u} = \boldsymbol{F} \qquad (1)$$

where $\boldsymbol{K}$ is the overall stiffness matrix of the structure, $\boldsymbol{u}$ is the nodal displacement vector, and $\boldsymbol{F}$ is the force vector acting on the nodes.

When the tunnel lining consists of a single closed ring without intersected elements, such as an interior column, the overall stiffness matrix of the structure is formulated as follows (Do, 2014; Do et al., 2020; Du et al., 2018, 2020a, b; Tien et al., 2020):

$$\boldsymbol{K} = \begin{bmatrix} \boldsymbol{k}_{n,d} + \boldsymbol{k}_{1,a} & \boldsymbol{k}_{1,b} & 0 & 0 & 0 & \boldsymbol{k}_{n,c} \\ \boldsymbol{k}_{1,c} & \boldsymbol{k}_{1,d} + \boldsymbol{k}_{2,a} & \boldsymbol{k}_{2,b} & 0 & 0 & 0 \\ 0 & \boldsymbol{k}_{2,c} & k_{2,d} + \boldsymbol{k}_{3,a} & \boldsymbol{k}_{3,b} & 0 & 0 \\ 0 & 0 & \boldsymbol{k}_{3,c} & \boldsymbol{k}_{3,d} + \boldsymbol{k}_{4,a} & \dots & 0 \\ 0 & 0 & 0 & \dots & \dots & \boldsymbol{k}_{n-1,b} \\ \boldsymbol{k}_{n,b} & 0 & 0 & 0 & \boldsymbol{k}_{n-1,c} & \boldsymbol{k}_{n-1,\mathrm{d}} + \boldsymbol{k}_{n,a} \end{bmatrix} \quad (2)$$

where $\boldsymbol{k}_{i,a}, \boldsymbol{k}_{i,b}, \boldsymbol{k}_{i,c}, \boldsymbol{k}_{i,d}$ are the sub-matrices corresponding to the ith element, each of which has a dimension of 3 × 3. The elemental stiffness matrix has the following form:

$$\boldsymbol{k}_{\mathrm{i}} = \begin{bmatrix} \boldsymbol{k}_{i,a} & \boldsymbol{k}_{i,b} \\ \boldsymbol{k}_{i,c} & \boldsymbol{k}_{i,d} \end{bmatrix} \quad (3)$$

However, for quasi-rectangular tunnels with an interior column, the intersection nodes between the column and the tunnel lining are connected to three beam elements: one element from the interior column and two elements from either side of the tunnel lining. The connection between the interior column and the lining is assumed to be rigid. In the numerical study, the tunnel lining is divided into 360 elements, while the interior column is composed of 11 elements, as depicted in Fig. 1. Consequently, the entire support structure consists of 371 elements and 370 nodes. Nodes 1 and 181, located at the bottom and the crown of the tunnel lining, respectively, represent the connection point between the interior column and the lining. The modified stiffness matrix for the tunnel structure, including the interior column, is described as follows:

$$\boldsymbol{K} = \begin{bmatrix} \boldsymbol{k}_{360,d} + \boldsymbol{k}_{361,a} + \boldsymbol{k}_{1,a} & \boldsymbol{k}_{1,b} & 0 & 0 & \dots & 0 & 0 \\ \boldsymbol{k}_{1,c} & \boldsymbol{k}_{1,d} + \boldsymbol{k}_{2,a} & \boldsymbol{k}_{2,b} & 0 & \dots & 0 & 0 \\ 0 & \boldsymbol{k}_{2,c} & \boldsymbol{k}_{2,d} + \boldsymbol{k}_{3,a} & \boldsymbol{k}_{3,b} & \dots & 0 & 0 \\ 0 & 0 & \boldsymbol{k}_{3,c} & \boldsymbol{k}_{3,d} + \boldsymbol{k}_{4,a} & \dots & 0 & 0 \\ \vdots & \vdots & \vdots & \vdots & \vdots & \vdots & \vdots \\ 0 & 0 & 0 & 0 & \dots & \boldsymbol{k}_{180,d} + \boldsymbol{k}_{181,a} + \boldsymbol{k}_{370,d} & \boldsymbol{k}_{181,b} \\ 0 & 0 & 0 & 0 & \dots & \boldsymbol{k}_{181,c} & \boldsymbol{k}_{181,d} + \boldsymbol{k}_{182,a} \\ \vdots & \vdots & \vdots & \vdots & \vdots & \vdots & \vdots \\ 0 & 0 & 0 & 0 & \dots & 0 & 0 \\ \boldsymbol{k}_{360,b} & 0 & 0 & 0 & \dots & 0 & 0 \\ \boldsymbol{k}_{361,c} & 0 & 0 & 0 & \dots & 0 & 0 \\ \vdots & \vdots & \vdots & \vdots & \vdots & \vdots & \vdots \\ 0 & 0 & 0 & 0 & \dots & 0 & 0 \\ 0 & 0 & 0 & 0 & \dots & \boldsymbol{k}_{370,b} & 0 \end{bmatrix}$$

$$\begin{bmatrix}
\cdots & 0 & \boldsymbol{k}_{360,c} & \boldsymbol{k}_{361,b} & \cdots & 0 & 0 \\
\cdots & 0 & 0 & 0 & \cdots & 0 & 0 \\
\cdots & 0 & 0 & 0 & \cdots & 0 & 0 \\
\cdots & 0 & 0 & 0 & \cdots & 0 & 0 \\
\vdots & \vdots & \vdots & \vdots & \vdots & \vdots & \cdots \\
\cdots & 0 & 0 & 0 & \cdots & 0 & \boldsymbol{k}_{370,c} \\
\cdots & 0 & 0 & 0 & \cdots & 0 & 0 \\
\vdots & \vdots & \vdots & \vdots & \vdots & \vdots & \vdots \\
\cdots & \boldsymbol{k}_{358,d}+\boldsymbol{k}_{359,a} & \boldsymbol{k}_{359,b} & 0 & \cdots & 0 & 0 \\
\cdots & \boldsymbol{k}_{359,c} & \boldsymbol{k}_{359,d}+\boldsymbol{k}_{360,a} & 0 & \cdots & 0 & 0 \\
\cdots & 0 & 0 & \boldsymbol{k}_{361,d}+\boldsymbol{k}_{362,a} & \cdots & 0 & 0 \\
\cdots & \cdots & \cdots & \cdots & \cdots & \cdots & \cdots \\
\cdots & 0 & 0 & 0 & \cdots & \boldsymbol{k}_{368,d}+\boldsymbol{k}_{369,a} & \boldsymbol{k}_{369,b} \\
\cdots & 0 & 0 & 0 & \cdots & \boldsymbol{k}_{369,c} & \boldsymbol{k}_{369,d}+\boldsymbol{k}_{370,a}
\end{bmatrix} \quad (4)$$

The normal and tangential spring stiffness (see Fig. 2), can be respectively determined through the normal and tangential stiffness of the soil with the average length of two adjacent elements:

$$k_{\mathrm{n},i} = \eta^*_{\mathrm{n},i}\frac{L_{i-1}+L_i}{2}W \quad (5)$$

$$k_{\mathrm{s},i} = \eta^*_{\mathrm{s},i}\frac{L_{i-1}+L_i}{2}W \quad (6)$$

where L_i is the length of the ith element; W is the unit length in the longitudinal direction of the considered element, usually taken as 1 m; and $\eta^*_{\mathrm{n},i}$ and $\eta^*_{\mathrm{s},i}$ are the apparent stiffness of the soil determined by the ratio of pressure to displacement in the normal and tangential directions at each node, respectively.

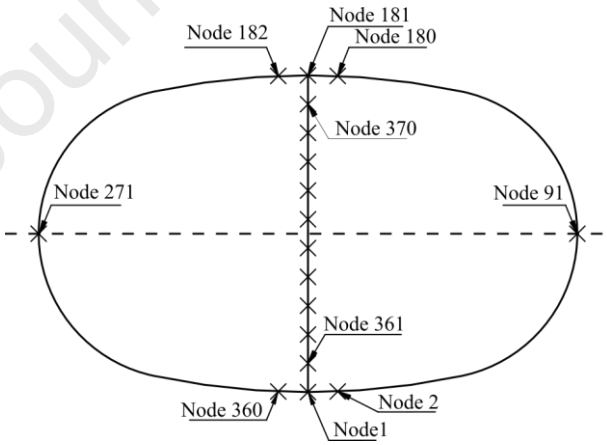

Fig. 1. Discretization of a quasi-rectangular tunnel's structures into beam elements and nodes (the '×' symbol denotes the node on the lining).

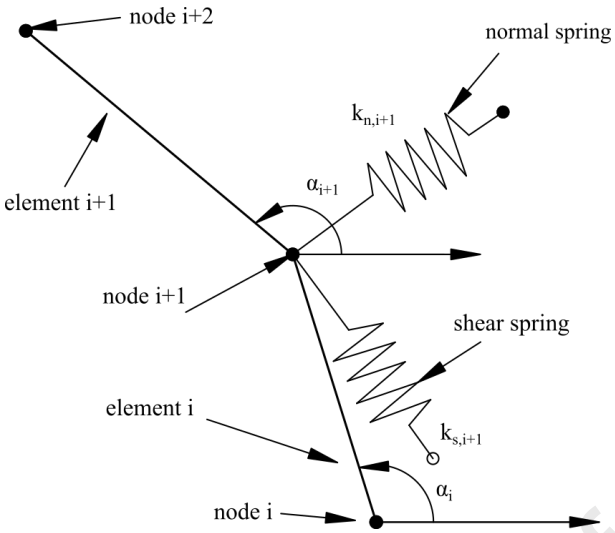

Fig. 2. The interaction between the ground and support through Winkler springs linked to the structure nodes.

It is important to note that the relationship between soil reaction pressure and structural displacement is generally nonlinear, as illustrated in Fig. 3. This applies to both the normal and tangential stiffness of the soil, as evidenced by the following equations (Oreste, 2007; Do et al., 2014).

$$\eta_{\mathrm{n},i}^{*} = \frac{p_{\mathrm{n},i}}{\delta_{\mathrm{n},i}} = \frac{p_{\mathrm{n,lim}}}{\delta_{\mathrm{n},i}}\left(1 - \frac{p_{\mathrm{n,lim}}}{p_{\mathrm{n,lim}} + \eta_{\mathrm{n},0}\delta_{\mathrm{n},i}}\right) \quad (7)$$

$$\eta_{\mathrm{s},i}^{*} = \frac{p_{\mathrm{s},i}}{\delta_{\mathrm{s},i}} = \frac{p_{\mathrm{s,lim}}}{\delta_{\mathrm{s},i}}\left(1 - \frac{p_{\mathrm{s,lim}}}{p_{\mathrm{s,lim}} + \eta_{\mathrm{s},0}\delta_{\mathrm{s},i}}\right) \quad (8)$$

where $p_{\mathrm{n,lim}}$ is the maximum normal reaction pressure determined by the friction angle (ϕ) and cohesion (c) of the soil. Taking into account the influence of the confining pressure $\Delta\sigma_{\mathrm{conf}}$, $p_{\mathrm{n,lim}}$ can be expressed as

$$p_{\mathrm{n,lim}} = \frac{2c\cos\phi}{1-\sin\phi} + \frac{1+\sin\phi}{1-\sin\phi}\Delta\sigma_{\mathrm{conf}} \quad (9)$$

$p_{\mathrm{s,lim}}$ is determined by the following expression:

$$p_{\mathrm{s,lim}} = \frac{\sigma_{\mathrm{h}}+\sigma_{\mathrm{v}}}{2}\tan\phi \quad (10)$$

where σ_{v} and σ_{h} are the vertical and horizontal loads, respectively.

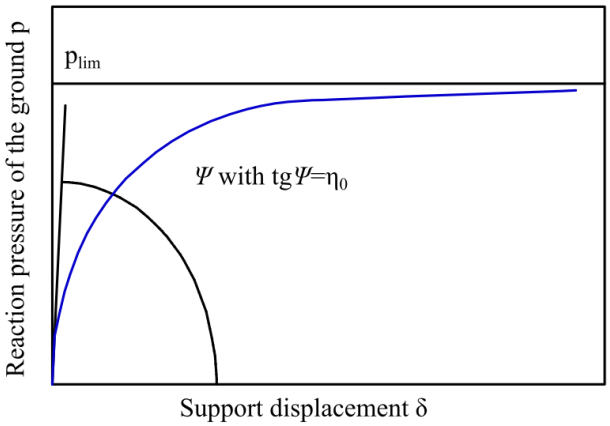

Fig. 3. Nonlinear relation between the reaction pressure of the ground (p) and the displacement of the support (δ). Ψ is the initial slope of the curve and is equal to arctan η_0 (Oreste, 2007).

$\eta_{n,0}$ in Eq. (7) is the initial normal stiffness of the soil, and $\eta_{s,0}$ in Eq. (8) is the initial tangential stiffness of the ground, which is taken as $\eta_{s,0}/3$ (Do et al., 2014). In this case, the value of $\eta_{n,0}$ is determined by the empirical equation (Möller, 2006):

$$\eta_{n,0} = \beta \frac{1}{1+\nu_s} \frac{E_s}{R_s} \qquad (11)$$

where ν_s is the Poisson's ratio of the soil, R_s is the radius of the corresponding arc in the quasi-rectangular tunnel cross-section, E_s is the Young's modulus of the soil, and β is a dimensionless factor.

The vertical load is determined according to Terzaghi's formula (Takano, 2000). If the overburden depth (H) of the tunnel exceeds twice the tunnel height H_t, i.e. $H > 2H_t$, the effective overburden depth can be utilized and determined by the following formula:

$$h_0 = \frac{B_1\left(1-c/B_1\gamma\right)}{K_0 \tan\phi}\left[1 - e^{-K_0 \tan\phi (H/B_1)}\right] + \frac{P_0}{\gamma} e^{-K_0 \tan\phi (H/B_1)} \qquad (12)$$

$$B_1 = B + H_t \cot\left(\frac{\frac{\pi}{4}+\frac{\phi}{2}}{2}\right) \qquad (13)$$

where γ represents the unit weight of the soil, K_0 denotes the lateral earth pressure coefficient, and B is the width of the quasi-rectangular tunnel.

The horizontal loads, denoted as σ_h and applied to the sidewall, are typically regarded as a specific proportion of the vertical loads, contingent upon the lateral earth pressure coefficient K_0 as

$$\sigma_h = K_0 \sigma_v \qquad (14)$$

As indicated by Terzaghi (1941), Blom (2002), Do and Dias (2018), and Kroetz et al. (2018), a reduction in the upward ground pressure acting on the bottom of the tunnel lining should be considered to account for the loss of the excavated soil's deadweight inside the tunnel. Based on a parametric investigation by comparing the HRM model with FEM calculations, this study

proposes a reduction factor of 0.81 for the upward pressure applied at the tunnel bottom.

2.2. Validation of the HRM model

The first quasi-rectangular tunnel, constructed as part of the Ningbo Metro Line 3 in Zhejiang, China (Liu et al., 2018b; Li et al., 2023b), is used as the reference case for validation purposes. The tunnel has a width of 11.5 m and a height of 6.937 m. The lining consists of 10 segments, labeled B1–B3, C1–C3, T1, T2, L, and F, and an interior column (LZ) (see Fig. 4). Segmental joints JF1–JF10 are present, however, in this study, the joint effect is not considered, and JF1–JF10 are treated as rigid joints. The lining and the interior column have a thickness of 450 mm and 350 mm, respectively. The tunnel is primarily formed by two arcs at the crown and invert, each covering an angle of 24°, and two arcs on the sides, each with an angle of 156°, as shown in Fig. 4.

Using the parameters of the Ningbo Metro Line 3, the proposed HRM model for the quasi-rectangular tunnel with an interior column was validated against FEM analysis (Plaxis, 2019).

The FEM model was assumed to be in plane strain, with a width and height of 100 m and 50 m, respectively. The computational mesh comprised approximately 17,000 15-node triangular elements and around 138,000 nodes. The bottom of the model was fixed in both vertical and horizontal displacements, while the lateral sides were allowed only vertical displacements. In contrast, the top of the model was allowed free displacements.

The soil behavior utilized in the FEM model follows the perfect Mohr–Coulomb (MC) plastic law. Although the MC model may not fully capture soil deformation as the hardening soil model (Celik, 2017; Chen and Peng, 2018; Miliziano and de Lillis, 2019), it is widely employed in studies involving the mechanical behavior of tunnel structures and preliminary design calculations due to its simplicity and sufficient accuracy (Abdellah et al., 2018; Miliziano and de Lillis, 2019; Vinod and Khabbaz, 2019; Karasev and Nguyen, 2022).

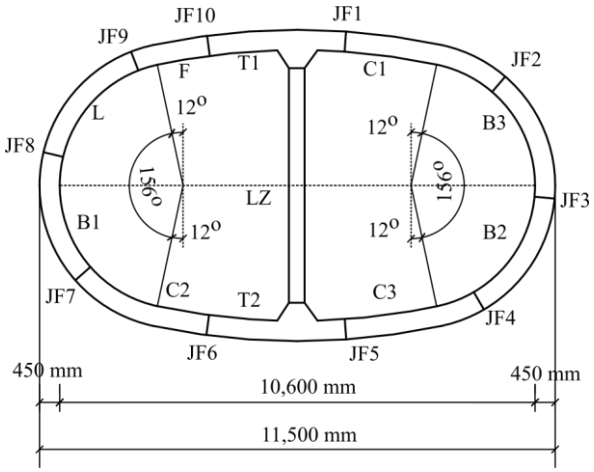

Fig. 4. Quasi-rectangular tunnel with an interior column of Ningbo metro line 3 (Case A) (Liu et al., 2018b).

Four scenarios of tunnel designs, labeled A, B, C, and D (see Table 1 and Figs. 4 and 5), are adopted for the validation purpose of the computational model. The tunnel designs in cases A and B have the same dimensions, but case A includes an interior column. Similarly, the tunnel in case C has the same dimensions as in case D, but case C includes an interior column. The tunnel lining is modeled using beam elements, with material parameters summarized in Table 2. For all calculations, the worst-case scenario is considered for the support structure without considering the deconfinement process of the surrounding soil before lining installation.

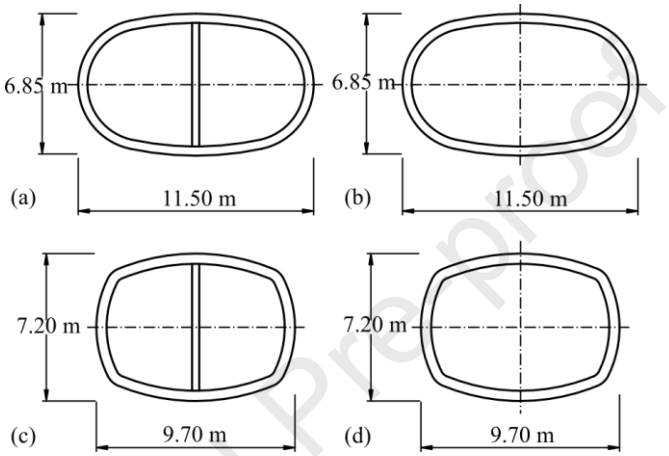

Fig. 5. Cases of quasi-rectangular tunnel: (a) Case A; (b) Case B; (c) Case C; and (d) Case D.

Table 1. Cross-sectional parameters of quasi-rectangular tunnel.

Parameter	Case	
	A and B	C and D
Tunnel width, B (m)	11.5	9.7
Tunnel height, H_t (m)	6.937	7.2
B/H_t	1.658	1.347
Outer perimeter, (m)	30.381	28.224
Outer area (m^2)	66.881	59.785

Table 2. Input parameters.

Parameter		Value
Properties of soil		
Unit weight, γ_s (kN/m^3)		18
Young's modulus, E_s (MPa)		3.6
Internal friction angle, ϕ ($^\circ$)		16.5
Cohesion, c (kPa)		25.6
Poisson's ratio, ν_s		0.35
Lateral earth pressure coefficient, K_0		$1 - \sin\phi$
Overburden, H (m)		10
Properties of tunnel lining		
Material model		Linear elastic
Young's modulus, E_1 (GPa)		31
Unit weight, γ_1 (kN/m^3)		24
Poisson's ratio, ν_1		0.15
Lining thickness (m)	Cases A and B	0.45

	Cases C and D	0.5
Thickness of the interior column (m)	All cases	0.35

The results obtained from the HRM and FEM models are depicted in Figs. 6 and 7 and Tables 3 and 4. These findings indicate that the HRM model matches closely with the FEM model in both the distribution and magnitude of internal forces within the support structure.

Remarkably, due to the presence of the interior column, the bending moment of the tunnel gradually shifts from positive to negative across the vault and reaches extreme values at the crown, as shown in Fig. 6. A similar pattern is also observed at the invert of the tunnel. As the tunnel width increases, the absolute value of the extreme bending moment also increases. This trend holds for both cases with (cases A and C) and without (cases B and D) an interior column. This behavior can be attributed to two factors: (1) the increased vertical loads as the tunnel width grows, which contributes to the loosening arching effect in the surrounding ground (Terzaghi, 1941); and (2) the greater flatness of the vault and bottom parts in cases A and B, which reduces the transformation effect of vertical loads to the tunnel sides.

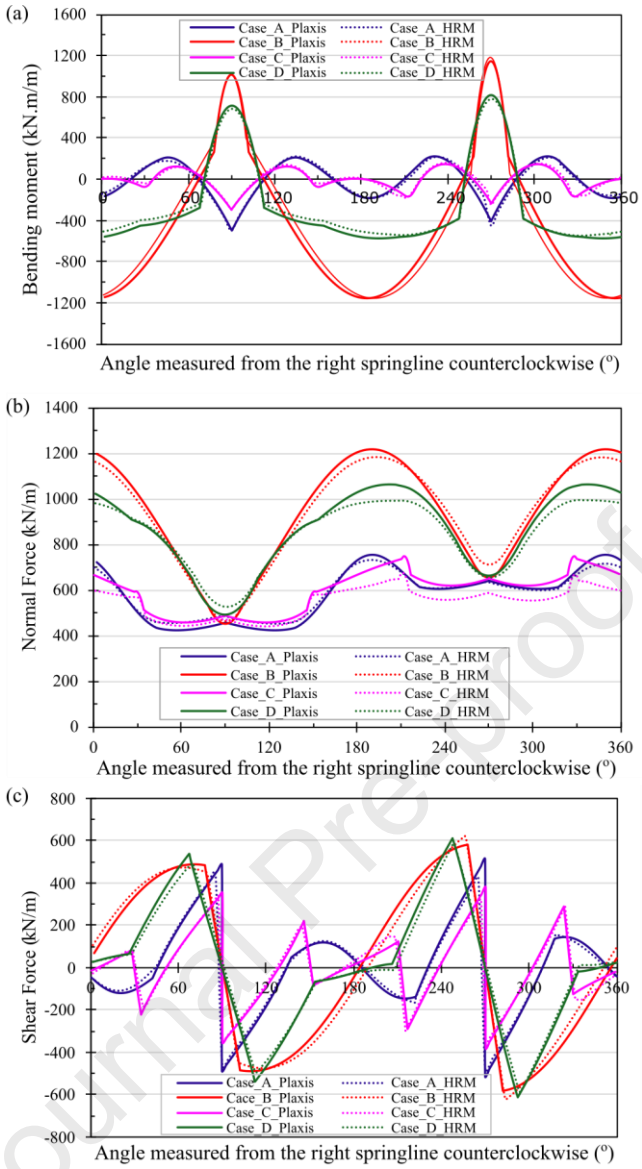

Fig. 6. Internal forces induced in quasi-rectangular tunnel lining: (a) Bending moment; and (b) Normal forces; c) Shear forces.

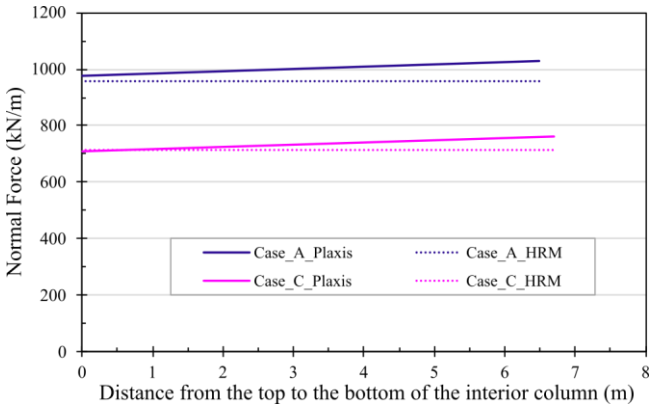

Fig. 7. Normal forces induced in the interior column.

The discrepancy in the maximum and minimum bending moments between the HRM and FEM models is very small, with a difference of less than 5% across all four tunnel cases. However, the variation in normal forces is slightly larger, ranging from 2% to 11%. In cases A and C, where the

tunnel structure includes an interior column acting as a central support under symmetrical loading, the bending moment and shear force within the column are negligible and are therefore not presented here for brevity.

Table 3. Comparison of extreme structural forces in the tunnel lining obtained by HRM and FEM.

Case	Maximum bending moment (kN m/m)			Minimum bending moment (kN m/m)			Maximum normal force (kN/m)		
	FEM	HRM	Difference (%)	FEM	HRM	Difference (%)	FEM	HRM	Difference (%)
A	224.03	227.22	1.42	-501.3	-501.39	0.02	754.63	731.8	-3.03
B	1150.94	1200.1	4.27	-1159.96	-1173	1.12	1218.44	1194.6	-1.96
C	151.6	153.88	1.5	-296.24	-300.36	1.39	749.72	672.78	-10.26
D	815.11	773.63	-5.09	-579.37	-552.43	-4.65	1062.06	996.45	-6.18
Case	Minimum normal force (kN/m)			Maximum shear force (kN/m)			Minimum shear force (kN/m)		
	FEM	HRM	Difference (%)	FEM	HRM	Difference (%)	FEM	HRM	Difference (%)
A	425.46	454.55	6.84	514.57	447.4	-13.05	-514.57	-483.01	-6.13
B	454.41	463.99	2.11	580.99	631.64	8.72	-580.99	-630.5	8.52
C	460.46	442.19	-3.97	381.45	338.26	-11.32	-381.45	-359.7	-5.7
D	489.99	527.82	7.72	612.27	587.4	-4.06	-612.26	-588.21	-3.93

Table 4. Comparison of extreme normal forces in the interior column obtained by HRM and FEM.

Case	Maximum value (kN/m)			Minimum value (kN/m)		
	FEM	HRM	Difference (%)	FEM	HRM	Difference (%)
A	1029.15	955.29	-7.18	977.26	955.29	-2.25
C	762.89	711.76	-6.7	709.29	711.76	0.35

Fig. 6 illustrates significant differences in internal forces within the tunnel structure between cases A and C, as well as cases B and D. The presence of an interior column drastically reduces both bending moments and normal forces. In case B (tunnel structure without an interior column), the maximum and minimum bending moments and the maximum normal force are 5.13, 2.31, and 1.62 times greater, respectively, compared to case A. Similar trends were also observed for cases C and D. The influence of the interior column on the distribution of bending moment is evident, particularly at the upper crown and lower invert sections of the tunnel lining, where the bending moment transitions from positive to negative values.

The interior column reduces the horizontal span of the tunnel structure, thereby increasing its overall stiffness, which in turn leads to a substantial reduction in internal forces. An interesting observation from Fig. 6a and b is that the presence of an interior column significantly diminishes the effect of tunnel shape and dimensions on internal forces. Indeed, while there are large differences in the bending moment and normal forces between cases B and D, much smaller discrepancies are observed between cases A and C, particularly at the crown, bottom, and sides of the tunnels. This can be attributed to the enhanced stiffness of the tunnel lining when an interior column is present.

The normal force results for the column, as shown in Fig. 7 (cases A and C), demonstrate that the HRM method exhibits a small deviation compared to the FEM results, with differences of less than 11%. The discrepancy in normal force is smaller at the top of the column than at the bottom. This can be attributed to the fact that, in the FEM method, the column's self-weight progressively

increases from top to bottom due to the effect of body load. As a result, the normal force increases along the column's height. In contrast, the HRM method does not account for the self-weight of the structure, resulting in a constant normal force throughout the column's height.

The above analysis reveals that the developed HRM model provides good agreement with the FEM computations in terms of internal forces for both cases (Tables 3 and 4). Therefore, the HRM analysis will be used for the parametric study and optimization of tunnel shape, which will be presented in the following sections.

2.3. Parametric study

Using the enhanced HRM model, an assessment was conducted to evaluate the impact of the interior column on the behavior of the quasi-rectangular tunnel lining concerning induced internal forces. The tunnel geometries for cases A and B were derived from the reference case of the Ningbo Metro Line 3. The parametric study included variations in soil Young's modulus (E_s), tunnel depth (H), lateral earth pressure coefficient (K_0), tunnel lining thickness (t_{lining}), and the thickness of the interior column (t_{column}). The outputs of interest are the maximum and minimum stresses on the tunnel lining under the critical state of the lining, i.e. under the maximum positive bending moment. A total of 88,935 simulations (including 8085 cases for a tunnel without an interior column) were performed using the HRM model, considering variations in the five input parameters. The ranges for these parameters are summarized in Table 5. The results indicate that the critical stresses in the tunnel lining can be reduced from a range of -140–146 MPa for tunnels without an interior column to -40–46 MPa with the installation of the interior column.

Table 5. Variation range of investigated parameters for the case of a quasi-rectangular tunnel.

Parameter	Value
H (m)	$1H_t$, $1.45H_t$, $2H_t$, $2.5H_t$, $3H_t$, $3.5H_t$, $4H_t$
E_s (MPa)	3.6, 10, 20, 30, 50, 75, 100, 150, 200, 250, 300
K_0	0.4, 0.6, 0.8, 1, 1.2
t_{lining} (m)	0.3, 0.32, 0.34, ..., 0.68, 0.7
t_{column} (m)	0.1, 0.2, 0.3, 0.4, 0.5, 0.6, 0.7, 0.8, 0.9, 1

The data obtained from HRM simulations were then utilized to study the influence of input parameters on system response for quasi-rectangular tunnels. To derive an input-output relationship prediction, the widely used ensemble ML algorithms, i.e. RF, gradient boosting decision tree (GBDT), extreme gradient boosting (XGBoost)), were employed. The accuracy of these prediction models was evaluated to determine the most effective one. In addition, a feature importance analysis was conducted using these ML models, and the outcomes were compared with engineering expectations to identify the most relevant input parameters for tunnels with

and without an interior column. Finally, the most accurate ML model and the most important features identified will be used to optimize the lining design.

3. ML for stress prediction in tunnel lining

The maximum and minimum stresses, representing compressive and tensile states in a cross-section, are determined based on the internal forces of the beam under loads, as outlined by Timoshenko (1976):

$$\sigma_{\max}^{\min} = \frac{N}{A} \pm \frac{M}{I} t/2 \qquad (15)$$

where A is the area of the considered cross-section, I is the inertia of the cross-section, and t is the thickness of the lining.

In this study, the critical section to be investigated is defined as the one with the largest positive bending moment. It should be noted that the tensile stress $\sigma_{\min}$ is not used to verify the limit state of the tunnel's concrete lining. Rather, it is used to assess the allowable tensile stress for the steel bars reinforcing within the concrete (ITA-WG2, 2019). Nevertheless, analyses of $\sigma_{\min}$ are still conducted to provide a comprehensive understanding of the tunnel lining's behavior under the impact of various input parameters.

3.1. Ensemble learning algorithms

In this section, three widely used ensemble ML algorithms (i.e. RF, GBDT, and XGBoost) are employed to establish ML models for the prediction of critical stresses in the tunnel lining.

3.1.1. RF

The first ML model, i.e. RF, combines a number of independent decision trees to create a "forest" (Breiman, 2001). By growing multiple decision trees, the accuracy of the prediction is improved. The training algorithm employed in RF is the bootstrap aggregation (bagging) method. In this approach, bootstrap subsets are randomly sampled from the original training set. For each subset, which can vary in the number of samples and features, a decision tree is constructed as a sub-prediction model, ensuring the diversity among the trees and mitigating the risk of overfitting. Each tree is grown until it reaches its maximum depth without pruning. In regression tasks, tree splits are determined based on variance reduction. The final prediction is obtained by averaging the outputs from all trees in the forest, as expressed by the following formula:

$$\boldsymbol{S} = \frac{1}{N} \sum_{n=1}^{N} \boldsymbol{S}_n(\boldsymbol{\Theta}) \qquad (16)$$

where $\boldsymbol{S}$ represents the average output of the prediction from a total of N trees; $\boldsymbol{\Theta}$ denotes the

input vector, and $\boldsymbol{S}_n(\boldsymbol{\Theta})$ stands for the individual prediction of a tree in the forest for an input vector. The hyperparameters in this algorithm are the number of trees and random features at each node, as well as the maximum depth of a tree.

3.1.2. GBDT

The GBDT approach enhances the robustness of predictions by aggregating the results of simpler learning models (Friedman, 2001). This aggregation is typically achieved by employing the boosting methods, where the base models, i.e. weak learners, are constructed using the decision tree (DT) learning algorithm. These DTs are sequentially combined to form the final model. Denoting $\boldsymbol{S}$ as the stress in the lining and $\boldsymbol{\Theta}$ as the tunnel parameters, a surrogate model based on GBDT can be defined as

$$\boldsymbol{S} = \boldsymbol{F}_W(\boldsymbol{\Theta}) = \sum_{w=1}^{W} f_w(\boldsymbol{\Theta}) \qquad (17)$$

where f_w is the wth weak DT model among the total of W weak models composing the final model. In each training iteration w, a new regression tree model $f_w(\boldsymbol{\Theta})$ is determined and added to the previous ensemble model $\boldsymbol{F}_{w-1}(\boldsymbol{\Theta})$ to constitute the current ensemble model $\boldsymbol{F}_w(\boldsymbol{\Theta})$. By minimizing the loss function $\boldsymbol{L}_w(\boldsymbol{\Theta})$ using the actual value $\boldsymbol{S}$ and the model output $\boldsymbol{F}(\boldsymbol{\Theta})$, the additive model f_w is obtained:

$$f_w(\Theta) = \underset{f_w(\boldsymbol{\Theta})}{\operatorname{argmin}} \sum_{m=1}^{M} \boldsymbol{L}_w\big(\boldsymbol{S}_m, \boldsymbol{F}_w(\boldsymbol{\Theta}_m)\big) = \underset{f_w(\boldsymbol{\Theta})}{\operatorname{argmin}} \sum_{m=1}^{M} \boldsymbol{L}_w\big(\boldsymbol{S}_m, \boldsymbol{F}_{w-1}(\boldsymbol{\Theta}_m) + f_w(\boldsymbol{\Theta}_m)\big) \qquad (18)$$

where $f_{\mathrm{w}}(\boldsymbol{\Theta}_m)$ represents the fitted simple DT model using the output $\boldsymbol{S}_m$ and the input $\boldsymbol{\Theta}_m$ of the data sample m ($1 \le m \le M$), with M denoting the total number of training samples. An approximation of the loss $\boldsymbol{L}_w(\boldsymbol{\Theta})$ using the first-order Taylor expansion is expressed as follows:

$$\boldsymbol{L}_w\big(\boldsymbol{S}_m, \boldsymbol{F}_{w-1}(\boldsymbol{\Theta}_m) + f_w(\boldsymbol{\Theta}_m)\big) \approx \boldsymbol{L}_w\big(\boldsymbol{S}_m, \boldsymbol{F}_{w-1}(\boldsymbol{\Theta}_m)\big) + g_w(\boldsymbol{\Theta}_m) f_w(\boldsymbol{\Theta}_m) \qquad (19)$$

where the first-order gradient $g_{\mathrm{w}}(\boldsymbol{\Theta}_{\mathrm{m}})$ is calculated as

$$g_w(\boldsymbol{\Theta}_m) = \left[\frac{\partial \boldsymbol{L}(\boldsymbol{S}_m, F(\boldsymbol{\Theta}_m))}{\partial \boldsymbol{F}(\boldsymbol{\Theta}_m)}\right]_{\boldsymbol{F}(\boldsymbol{\Theta}) = \boldsymbol{F}_{w-1}(\boldsymbol{\Theta})} \qquad (20)$$

By inserting Eq. (19) into Eq. (18) and removing the constant error $\boldsymbol{L}_w$ between $\boldsymbol{S}_m$ and the output of the previous ensemble model $\boldsymbol{F}_{w-11}(\boldsymbol{\Theta}_m)$, the minimization yields

$$f_w(\boldsymbol{\Theta}) = \underset{f_w(\boldsymbol{\Theta})}{\operatorname{argmin}} \sum_{m=1}^{M} g_w(\boldsymbol{\Theta}_m)\, f_w(\boldsymbol{\Theta}_m) \qquad (21)$$

At each iteration w, the negative gradients of data samples $-g_w(\boldsymbol{\Theta}_m)$ are calculated based on the fitted model $f_w(\boldsymbol{\Theta}_m)$.

3.1.3. XGBoost

While the GBDT method constructs weak learning models using fixed-sized DTs in a stage-wise, time-consuming greedy strategy, XGBoost improves GBDT in both efficiency and scalability. XGBoost achieves this improvement through parallel boosting and regularization

techniques, which help to reduce the risk of overfitting during the training process (Chen and Guestrin, 2016). The objective function to be minimized in XGBoost is expressed as

$$\boldsymbol{J}(\boldsymbol{\Theta}) = \boldsymbol{L}_w(\boldsymbol{\Theta}) + \Omega \quad (22)$$

where Ω denotes the regularization term. In the XGBoost model, both L1 (Lasso) and L2 (Ridge) regularization are incorporated into Ω, thereby enhancing model generalization and reducing overfitting. The regularization term Ω of a tree with Q leaves is defined as

$$\Omega = \gamma Q + \frac{1}{2}\lambda \sum_{j=1}^{Q} \boldsymbol{\omega}_j^2 \quad (23)$$

where γ is the penalty for several leaves; λ stands for the L2 regularization term on leaf weights, and $\boldsymbol{\omega}^2$ represents the weight of the jth leaf. In addition, to improve the minimization efficiency, the second-order Taylor expansion is adopted to compute the loss $\boldsymbol{L}_w(\boldsymbol{\Theta})$ in Eq. (19) as

$$\boldsymbol{L}_w(\boldsymbol{\Theta}_m) \approx \boldsymbol{L}_w\left(\boldsymbol{S}_m, \boldsymbol{F}_{w-1}(\boldsymbol{\Theta}_m)\right) + g_w(\boldsymbol{\Theta}_m) f_w(\boldsymbol{\Theta}_m) + \frac{1}{2} h_w(\boldsymbol{\Theta}_m) f_w^2(\boldsymbol{\Theta}) \quad (24)$$

where $h_w(\boldsymbol{\Theta})$ denotes the second-order gradient. By considering both the first- and second-order derivatives, XGBoost enables more informed decisions about splits, which often result in better feature selection. Concerning the feature splitting in building a decision tree, GBDT suffers from potential loss for all possible features when they are split to create a new branch of the tree. XGBoost addresses this inefficiency by adopting an approximation approach. In the approximation procedure, the distribution of features (histograms) across all data points in a leaf is taken into account to reduce the search space of possible feature splits. The splitting can be decided globally a priori at the beginning of the training or locally for each leaf to accelerate the training process.

3.2. Evaluation of prediction capabilities

In this section, the effects of three ML models (RF, GBDT, and XGBoost) on the prediction of the maximum ($\sigma_{\max}$) and minimum ($\sigma_{\min}$) stresses of the quasi-rectangular tunnel lining with and without an interior column are examined. The performance of each ML model is evaluated based on a 5-fold cross-validation, in which the dataset is divided into five sub-datasets of equal size. In each validation, the prediction quality of the ML model is quantified by comparing the predicted and the HRM reference results using two metrics: the well-known coefficient of determination (R^2) and the mean absolute percentage error (MAPE):

$$MAPE = \frac{1}{N}\sum_{i=1}^{N}\left|\frac{\sigma_i^{\mathrm{HRM}} - \sigma_i^*}{\sigma_i^{\mathrm{HRM}}}\right| \times 100\% \quad (25)$$

3.2.1. Without the interior column

To investigate this specific case, 8085 simulations were used for the training and testing of the ML models. The corresponding four inputs are H, E_s, K_0, and t_{lining}. The optimal hyperparameters (max_depth and n_estimators) for the configuration of each ML model are determined using the

grid search algorithm (Tang and Na, 2021). The mean MAPE and R^2 of all validation cases in each fold, as well as the average performance of the 5-fold validation corresponding to each ML model, are given in Tables 6 and 7 for the prediction of $\sigma_{\max}$ and $\sigma_{\min}$, respectively. In this section, the effect of each input feature on each output, i.e. $\sigma_{\max}$ and $\sigma_{\min}$, is studied separately with individual ML models.

Concerning the prediction of $\sigma_{\max}$, the RF model indicates a good prediction, with an error of *MAPE* = 5.48% and R^2 = 0.983. The XGBoost model shows a significant improvement in the prediction accuracy, with *MAPE* = 1.08% and R^2 = 0.999. However, the GBDT model exhibits the best prediction in this case, with R^2 = 0.999 and *MAPE* = 0.76%.

A similar trend is evident in the prediction of $\sigma_{\min}$ for the tunnel lining, as shown in Table 7. The performance difference between the GBDT and XGBoost models is almost negligible, with both achieving average R^2 values of 0.999 and average MAPE values of 0.86% and 1.28%, respectively, over 5-fold cross-validation. However, XGBoost significantly outperforms GBDT in terms of computation time, taking only 1.5 s compared to GBDT's 12.9 s, representing a nearly ninefold reduction. Both boosting-based models outperform the RF model, which has a MAPE of 6.24% and an R^2 of 0.982, in predicting $\sigma_{\min}$.

Table 6. Optimum hyperparameters and prediction accuracy of three ML models for $\sigma_{\max}$ using 8085 simulations of a tunnel without an interior column.

ML model	Optimum parameters		R^2 of 5-fold cross-validation						MAPE of 5-fold cross-validation (%)						Time (s)
	max_depth	n_estimators	1	2	3	4	5	Average	1	2	3	4	5	Average	
RF	8	50	0.981	0.984	0.983	0.982	0.983	0.983	5.5	5.4	5.2	6.0	5.3	5.48	2.37
GBDT	8	200	0.999	0.999	0.999	0.999	0.999	0.999	0.7	0.8	0.8	0.7	0.8	0.76	12.93
XGBoost	8	200	0.999	0.999	0.999	0.999	0.999	0.999	1	1.2	1.1	1	1.1	1.08	1.7

Table 7. Optimum hyperparameters and prediction accuracy of three ML models for $\sigma_{\min}$ using 8085 simulations of a tunnel without an interior column.

ML model	Optimum parameters		R^2 of 5-fold cross-validation						MAPE of 5-fold cross-validation (%)						Time (s)
	max_depth	n_estimators	1	2	3	4	5	Average	1	2	3	4	5	Average	
RF	8	50	0.983	0.981	0.983	0.98	0.981	0.982	6.2	6.2	6.2	6.5	6.1	6.24	2.54
GBDT	8	200	0.999	0.999	0.999	0.999	0.999	0.999	0.9	0.8	0.9	0.9	0.8	0.86	12.89
XGBoost	8	100	0.999	0.999	0.999	0.999	0.999	0.999	1.2	1.4	1.2	1.3	1.3	1.28	1.5

3.2.2. With the interior column

A total of 80,850 simulations were conducted for a tunnel with an interior column. In addition to the four inputs used in the case without an interior column, the thickness of the interior column (t_{column}) was also considered. The model outputs remain $\sigma_{\max}$ and $\sigma_{\min}$. The corresponding performance of the investigated ML models is given in Tables 8 and 9.

Table 8. Optimum hyperparameters and prediction accuracy of three ML models for $\sigma_{\max}$ using 80,850 simulations of a tunnel with an interior column.

ML model	Optimum parameters		R^2 of 5-fold cross-validation						MAPE of 5-fold cross-validation (%)						Time (s)
	max_depth	n_estimators	1	2	3	4	5	Average	1	2	3	4	5	Average	
RF	8	50	0.993	0.993	0.993	0.993	0.993	0.993	2.4	2.5	2.5	2.5	2.5	2.48	21.95
GBDT	8	200	0.999	0.999	0.999	0.999	0.999	0.999	0.21	0.21	0.21	0.21	0.21	0.21	133.2
XGBoost	8	200	0.999	0.999	0.999	0.999	0.999	0.999	0.4	0.4	0.4	0.4	0.4	0.4	4.7

Table 9. Optimum hyperparameters and prediction accuracy of 3 ML models for $\sigma_{\min}$ using 80,850 simulations of a tunnel with the interior column.

ML model	Optimum parameters		R^2 of 5-fold cross-validation						MAPE of 5-fold cross-validation (%)						Time (s)
	max_depth	n_estimators	1	2	3	4	5	Average	1	2	3	4	5	Average	
RF	8	50	0.986	0.987	0.987	0.987	0.987	0.987	3.4	3.5	3.4	3.5	3.5	3.46	21.98
GBDT	8	200	0.999	0.999	0.999	0.999	0.999	0.999	0.27	0.27	0.27	0.27	0.27	0.27	140.7
XGBoost	8	200	0.999	0.999	0.999	0.999	0.999	0.999	0.4	0.4	0.4	0.4	0.4	0.4	5.5

The results demonstrate that all ML models provide excellent predictions for both $\sigma_{\max}$ and $\sigma_{\min}$ with $R^2 \approx 0.99$. In particular, for the prediction of $\sigma_{\max}$, the RF model shows the lowest accuracy, with an average MAPE of 2.48%. In contrast, the GBDT provides the highest accuracy with an average MAPE of 0.21%, as shown in Table 8. However, it is the most computationally expensive model, requiring a computation time of 133.2 s. The XGBoost model, while exhibiting slightly reduced accuracy ($MAPE$ = 0.4%), is much more computationally efficient, with a computation time of only 4.7 s. For $\sigma_{\min}$, both the GBDT and XGBoost models exhibit excellent performance, with average MAPE values of 0.27% and 0.4%, respectively. However, the computation time for GBDT (140.7 s) is significantly longer than that for XGBoost (5.5 s). In contrast, the RF model is the least effective for predicting $\sigma_{\min}$, with an average MAPE of 3.46% and a computation time of 21.98 s.

The results presented in this section demonstrate that XGBoost is the most efficient model for the prediction of stress on tunnel lining, both with and without interior columns. This model is then utilized to extract feature importance to reveal the impact of input features on the predicted stress outputs, which will be presented in the next section.

4. Feature importance analysis

4.1. Analysis methods

This section focuses on analyzing the importance of input features in predicting stresses in the tunnel lining. Given that the ML models discussed in Section 3 are often regarded as black-box models and difficult to interpret, SHAP (explainable artificial intelligence) is employed to clarify the input-output relationships. Furthermore, two commonly used feature importance techniques, namely mean decrease impurity-based feature importance (MDI) and permutation feature importance (PFI), are also investigated and compared.

4.1.1. SHAP

The SHAP method, based on the game theory approach (Lundberg and Lee, 2017), is typically used to estimate the influence of selected features on the quality of output predictions. SHAP enhances the transparency and interpretability of the input-output relationship in the data by

assigning an importance value to each input feature, which reflects its effect on the model. In this study, features with larger absolute values are considered more important. TreeSHAP, a variant of SHAP for tree-based ML models, is employed. The Shapley values of a tree ensemble represent the global importance and are calculated as the weighted average of the Shapley values from individual trees, as described in the following equation:

$$s_i = \frac{1}{M}\sum_{m=1}^{M}|\phi_i^m| \quad (26)$$

where ϕ^m denotes the attribution of the *i*th feature using the sample m in the M samples.

4.1.2. Mean decrease in impurity

The MDI is a measure for the importance ranking of input features, which is computed from statistics derived from the training dataset of an ML model. MDI is particularly useful for examining overfitted models when the importance is high even for features of the target variable in the test set that are not predictive. By incorporating MDI, the XGBoost model in this study can be better generalized to improve the reliability of the feature analysis. Furthermore, the importance indices are calculated as the average values over a 5-fold cross-validation, which further improves the model's generalization. As described by Breiman (2001), the global feature importance s_i for the *i*th feature is calculated by averaging the local importance s_i^k across all the K data samples as follows:

$$s_i = \sum_{k=1}^{K}\left|s_i^k\right| = \sum_{k=1}^{K}\frac{1}{T}\sum_{t=1}^{T}\left|f_{t,i}^k\right| \quad (27)$$

where K denotes the total number of samples; $f_{t,i}^k$ is the feature value of the tree t in the tree-based model, i.e. XGBoost; and T is the total number of trees.

4.1.3. PFI

In contrast to MDI, PFI evaluates the contribution of each feature to the statistical performance of a fitting model on a given dataset (Breiman, 2001). The permutation importance of a feature is determined by comparing the baseline score metric s of an original dataset to the new score metric s_i obtained after permuting the *i*th feature column. The rationale of this approach is to break the relationship between the feature and the target variable by randomly shuffling the value of a single feature. As a result, the decrease in the model's score can reveal how much it depends on a particular feature. Considering N repetition of the permutation process, the importance value of the *i*th feature can be calculated as

$$s_i = s - \frac{1}{N}\sum_{i=1}^{N} s_{n,i} \quad (28)$$

To avoid any potential bias, i.e. model dependence, and improve the model's generalization, the PFI is carried out on all three ML models, namely RF, GBDT, and XGBoost.

4.2. Analysis results

4.2.1. Without the interior column

Fig. 8a illustrates the contribution of each feature to σ_{max}. It is evident that E_s has the most significant impact, while the importance of the three features, namely H, K_0, and t_{lining}, is quite similar. Although both the PFI and SHAP methods yield comparable importance values for H and t_{lining}, the MDI approach indicates that H is of greater consequence than t_{lining}. This discrepancy can be attributed to the model dependency of the MDI approach, whereas results from PFI and SHAP are averaged based on results from different models (RF, GBDT, and XGBoost), thus leading to a higher degree of generalization and model independence. However, all three feature importance analysis methods agree that K_0 is the least impact factor in predicting σ_{max}.

A similar trend of importance ranking for σ_{min} can be observed in Fig. 8b, where E_s is again the most important feature for predicting σ_{min}. While MDI ranks t_{lining} as the least influential factor for σ_{min}, SHAP and PFI rank it as a more important feature. Furthermore, these two methods also rank H as the least influential feature for σ_{min}, which differs from the ranking of K_0 for σ_{max}.

In summary, the three methods investigated for determining feature importance yield similar results and show good agreement in the case without an interior column. The importance degrees of the four features are almost comparable for both σ_{max} and σ_{min} predictions, with all methods ranking E_s as the most important factor for predicting critical stresses. However, the rankings of H, K_0, and t_{lining} are not clearly distinguishable and thus indecisive.

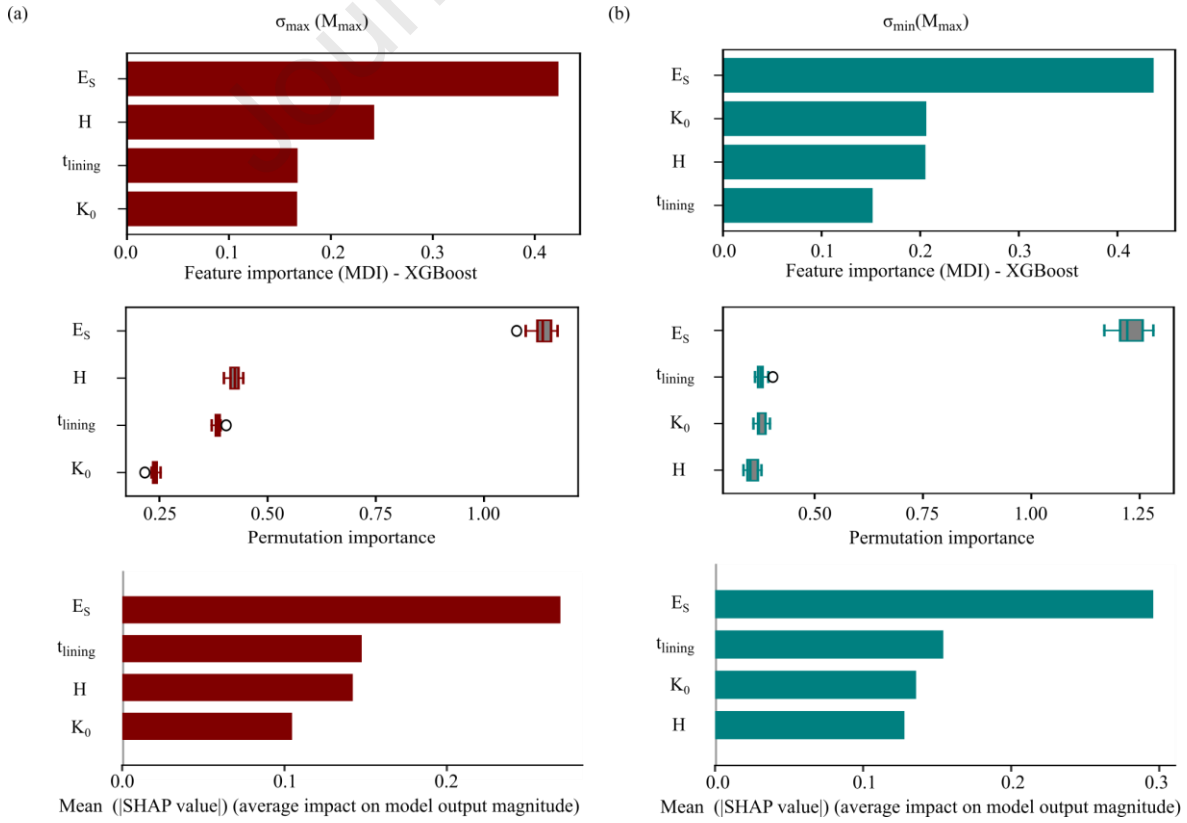

Fig. 8. Effects of input features on the critical stresses in the tunnel lining using MDI, PFI, and SHAP in case of a tunnel without an interior column: (a) σ_{max}; and (b) σ_{min}.

4.2.2. With an interior column

In the second feature analysis, t_{column} is introduced as an additional input to examine the role of the interior column in predicting critical stresses in the tunnel lining. The ML models used in this analysis are described in Section 3.2.2. Fig. 9 illustrates the contribution of each feature to the output in the simulation dataset for the case with an interior column. Unlike the case without the interior column, the ranking results from all three feature importance approaches are in alignment for both σ_{max} and σ_{min}, except MDI, where t_{column} and t_{lining} alternate as the least important factors. Despite this, all methods consistently evaluate that the depth H is the most influential factor for predicting critical stresses, with K_0 now ranked second. In contrast, E_s is ranked third, instead of the leading role observed in the case without an interior column. In particular, the SHAP analysis indicates that the influence of t_{column} on the critical stresses is minor. Conversely, the effect of t_{lining} on σ_{max} is slightly more pronounced. It is anticipated that, given the thickness of the column, its stiffness will be sufficient to restrain the deflection of the tunnel's vault and bottom. Moreover, the normal forces in the interior column, as shown in Fig. 7, indicate that the maximum compressive stress is always below the yield stress of C35/45 concrete, which is commonly used in lining construction. This observation, combined with the feature importance analysis in this section, suggests that t_{column} should be selected based on the required structural slenderness ratio rather than material strength. Further details on this are provided in Section 5.

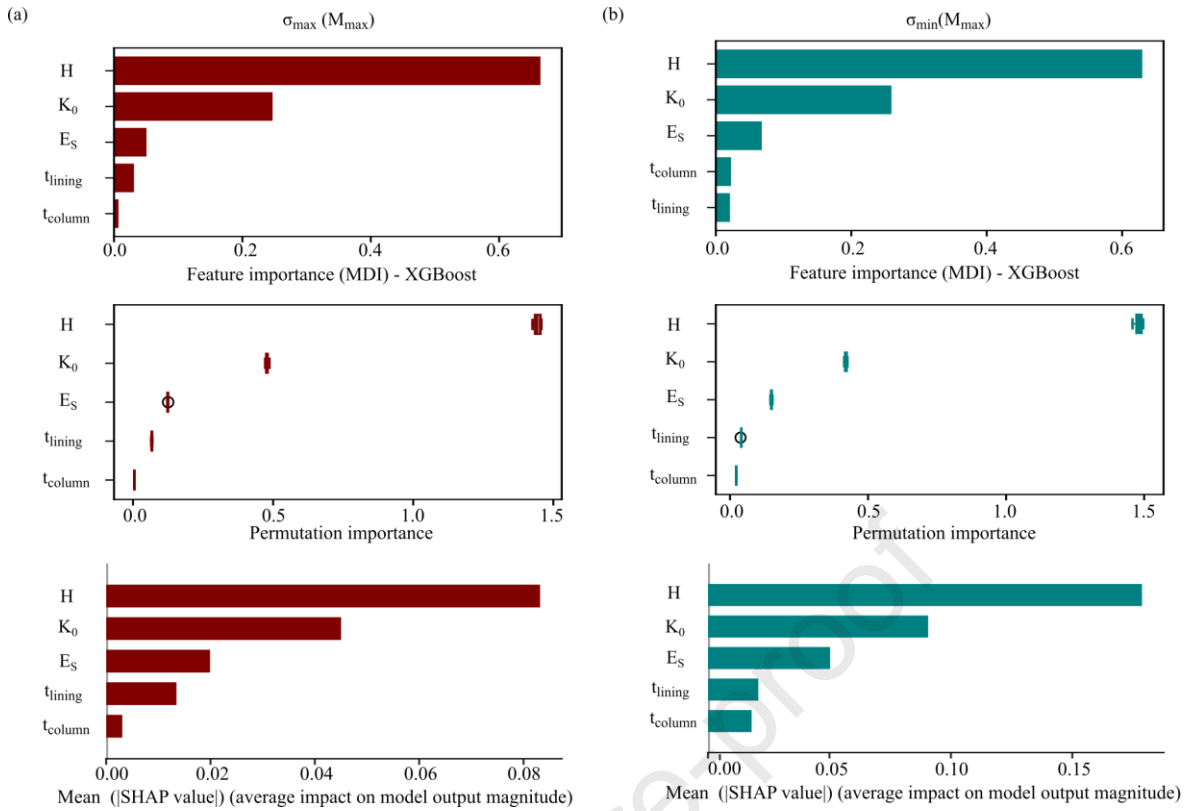

Fig. 9. Effects of input features on the critical stresses in the tunnel lining using MDI, PFI, and SHAP in case of a tunnel with an interior column: (a) σ_{max}; and (b) σ_{min}.

4.2.3. Verification of the requirement of the interior column

Although t_{column} has a minor impact on critical stresses, omitting the interior column would significantly alter the stress profile, leading to greater displacement and bending moment at the tunnel crown and bottom.

To verify this, the feature analysis from Section 4.2.2 is repeated, replacing t_{column} with a new binary parameter (*Yes/No column*) to indicate the existence of the interior column in the HRM analysis. The simulations used in the previous case studies in Sections 4.2.1 and 4.2.2 are combined to create a dataset comprising 88,935 simulations for feature analysis. Subsequently, the respective five inputs are H, E_s, K_0, t_{lining}, and *Yes/No column* indicator. As the dataset has been changed, new ML models must be created according to the method described in Section 3.2. All the ML models are trained to achieve R^2 values greater than 0.99 to ensure the reliability of the predictions.

As shown in Fig. 10, the interior column significantly affects σ_{max}, but has a minimal effect on σ_{min}. For the prediction of σ_{min}, the result is consistent with the previous investigation (see Fig. 9b), where H remains the most important factor. Additionally, the importance of other features, i.e. H, K_0, E_s, and t_{lining}, is re-ranked, showing a balanced contribution between the scenarios with and without the interior column. Nevertheless, as the interior column has been demonstrated to

be a significant factor influencing σ_{max}, which plays a crucial role in the stability of the tunnel lining, it is essential to incorporate this element into the design process. The subsequent section will examine an optimization strategy for the quasi-rectangular tunnel.

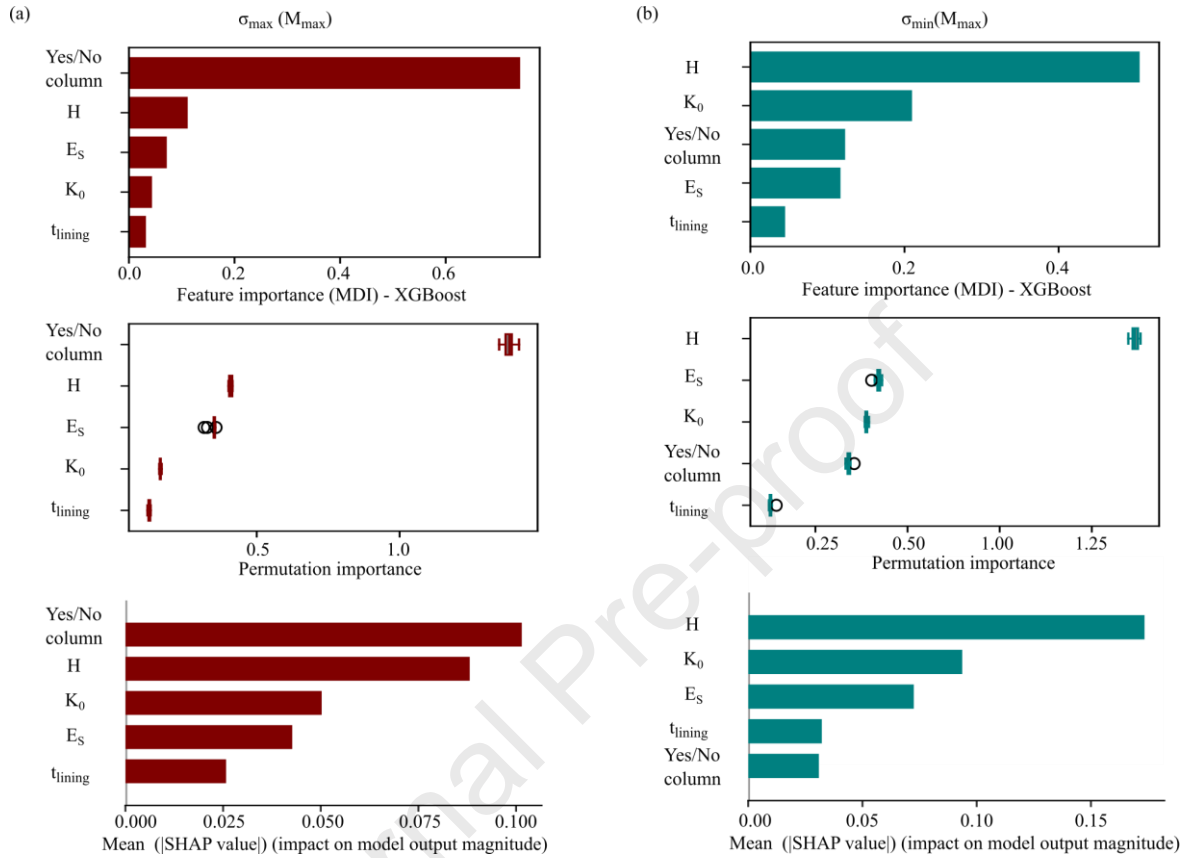

Fig. 10. Effects of input features on the critical stresses in the lining using MDI, PFI, and SHAP in case of tunnels with and without an interior column: (a) σ_{max}; and (b) σ_{min}.

5. Optimization of lining design

Considering the necessity of an interior column in a quasi-rectangular tunnel, it is pertinent to determine the appropriate column thickness to keep the critical stresses within predefined bounds. Although H is identified as the most influential parameter when the column is installed, it is typically not a design parameter, as the tunnel depth is usually constrained. Similarly, K_0 and E_s are largely influenced by ground characteristics and therefore not considered design variables. This leaves two design parameters: t_{lining} and t_{column}.

In this section, a multi-objective constraint optimization problem is addressed to estimate the optimal thicknesses for the tunnel lining and column. During the analysis, the depth of the tunnel H, Young's modulus of soil E_s, and the lateral earth pressure coefficient K_0 are held constant, while t_{lining} and t_{column} are optimized. Considering the high cost of materials, optimizing these two parameters, i.e. t_{lining} and t_{column}, is beneficial to minimize the cost. Subsequently, the fitness,

i.e. the cost function, of the optimization problem is defined as the minimization of $\sigma_{\max} = f(t_{\text{lining}}, t_{\text{column}})$, where f is the response function obtained from the ML model. The constraint on $\sigma_{\max}$ is based on the maximum allowable compressive stress according to Eurocode EN 1992-1-1:2004 (2004), and must remain within specified stress limits:

$$\left.\begin{array}{ll} \min & (\sigma_{\max}; t_{\text{lining}}; t_{\text{column}}) \\ \text{s.t.} & \sigma_{max} = f(t_{\text{lining}}; t_{\text{column}}) \le 0.6 f_c \approx 26 \text{ MPa} \\ & 0.3 \le t_{\text{lining}} \le 0.7 \\ & 0.1 \le t_{\text{column}} \le 1 \end{array}\right\} \quad (29)$$

where f_c = 43 MPa is the mean cylinder compressive strength of concrete C35/45. As previously stated, the tensile stress $\sigma_{\min}$ is employed exclusively to design the steel mesh installed in the concrete lining. Therefore, only the compressive stress $\sigma_{\max}$ is considered in the optimization of the lining in this section (ITA-WG2, 2019).

The optimization is performed for both cases without and with the interior column. In the former case, the variable t_{column} is not relevant. The well-known PSO algorithm is employed for the optimization with the specified constraints. In addition, a deterministic mapping model is required to predict the input-output relationship. XGBoost models from Sections 3.2.1 and 3.2.2 are therefore employed to accelerate the optimization process instead of the expensive HRM analysis. As shown in Section 4, t_{lining} has a more significant impact on the compressive stress $\sigma_{\max}$ than t_{column}, and thus it is assigned a higher priority in the study with an interior column.

5.1. PSO

The main idea of PSO is to identify an optimal solution $\left[t^{\text{opt}}_{\text{lining,}}, t^{\text{opt}}_{\text{column,}}\right]$ to a given problem based on the theory of swarm movement. The process begins with an initialization of random solutions obtained from P possible candidates (particles) of a swarm $\boldsymbol{X}$:

$$\boldsymbol{X} = (x_1, x_2, \dots, x_p) \quad (p = 1,2, \dots, P) \quad (30)$$

In a two-dimensional space or an input space with two parameters t_{lining} and t_{column}, the random position of a particle p is defined as

$$x_p = \left[t^p_{\text{lining}}, t^p_{\text{column}}\right] \quad (p = 1,2, \dots, P) \quad (31)$$

$$\boldsymbol{X} = \left[t^1_{\text{lining}}, t^1_{\text{column}}\right], \left[t^2_{\text{lining}}, t^2_{\text{column}}\right], \dots, \left[t^P_{\text{lining}}, t^P_{\text{column}}\right] \quad (32)$$

The optimized solution $\left[t^{\text{opt}}_{\text{lining}}, t^{\text{opt}}_{\text{column}}\right]$ is obtained by iteratively improving candidate solutions with respect to a given quality measure. At each iteration, the global optimum position $\left[t^{\text{g}}_{\text{lining}}, t^{\text{g}}_{\text{column}}\right]$ among the particles of the swarm is identified. The global position is then identified as the target to which the particles are to be moved by continuously updating the position $\left[t^{p}_{\text{lining}},\right.$

$t^p_{\text{column}}\Big]^{(t+1)}$ and velocity $\left[v^p_{\text{lining}}, v^p_{\text{column}}\right]^{(t+1)}$ of the particles at the next iteration as follows:

$$\left[t^p_{\text{lining}},\ t^p_{\text{column}}\right]^{(t+1)} = \left[t^p_{\text{lining}},\ t^p_{\text{column}}\right]^{(t)} + \left[v^p_{\text{lining}},\ v^p_{\text{column}}\right]^{(t+1)} \quad (33)$$

$$\left[v^p_{\text{lining}},\ v^p_{\text{column}}\right]^{(t+1)} = \left[v^p_{\text{lining}},\ v^p_{\text{column}}\right]^{(t)} + c_1\left(\left[t^{p,\text{l}}_{\text{lining,}},\ t^{p,\text{l}}_{\text{column}}\right] - \left[t^p_{\text{lining}},\ t^p_{\text{column}}\right]^{(t)}\right)r_1 + c_2\left(\left[t^{\text{g}}_{\text{lining}},\ t^{\text{g}}_{\text{column}}\right] - \left[t^p_{\text{lining}},\ t^p_{\text{column}}\right]^{(t)}\right)r_2 \quad (34)$$

The movement gradient or the velocity of particle p is not only guided towards the global position $\left[t^{\text{g}}_{\text{lining}}, t^{\text{g}}_{\text{column}}\right]$ in the search space, but is also strongly influenced by its local best position $\left[t^{p,\text{l}}_{\text{lining,}}, t^{p,\text{l}}_{\text{column}}\right]$. The acceleration coefficients c_1 and c_2, which control the magnitude of the moving step of the particle towards the $\left[t^{p,\text{l}}_{\text{lining,}}, t^{p,\text{l}}_{\text{column}}\right]$ and $\left[t^{\text{g}}_{\text{lining}}, t^{\text{g}}_{\text{column}}\right]$, respectively, typically range between 0 and 4. Meanwhile, the values of r_1 and r_2 are randomly generated with a uniform distribution in [0,1] to consider the stochastic influence on the velocity update rule. The algorithm is repeated until a stopping criterion, such as a maximum number of iterations or a predefined tolerance, is fulfilled. Finally, all particles in the swarm are expected to converge towards the optimal solution.

5.2. Optimization results

5.2.1. Without the interior column

In the PSO optimization, only the design variables can be adjusted. In this case, only t_{lining} is subjected to alteration. The remaining input parameters, including H, E_{s}, and K_0, are fixed. To illustrate the proposed methodology, a case study was conducted with the following parameters: $H = 4H_{\text{t}}$, E_{s} = 50 MPa, and K_0 = 0.6. The PSO algorithm was configured with 25 particles and a maximum of 100 iterations. At the initial iteration, the t_{lining} values for all 25 particles of the swarm were randomly generated within the range of 0.3–0.7 m, using a uniform distribution.

Fig, 11 shows the convergence plot of t_{lining}, in which the t_{lining} values of each particle are represented by blue dots. The fitness function, i.e. σ_{max} in the tunnel lining, is then calculated using the XGBoost model and plotted as the vertical coordinate corresponding to each thickness value. The green line in Fig. 11 represents the stress limit (26 MPa), which denotes the upper bound of σ_{max}. The results reveal that, at iteration 5, all particles are moving towards the upper bound of t_{lining}, and converge at iteration 20, where they are all gathered around the solution of $t_{\text{lining}} \approx 0.66$ m and $\sigma_{\text{max}} \approx 25.8$ MPa. This optimal value is noteworthy, as it is demonstrated that a substantial lining thickness may be required to constrain the maximum stress within the standard bounds. This highlights again the necessity to install the interior column for sub-

rectangular tunnels, a topic that will be further explored in the subsequent section.

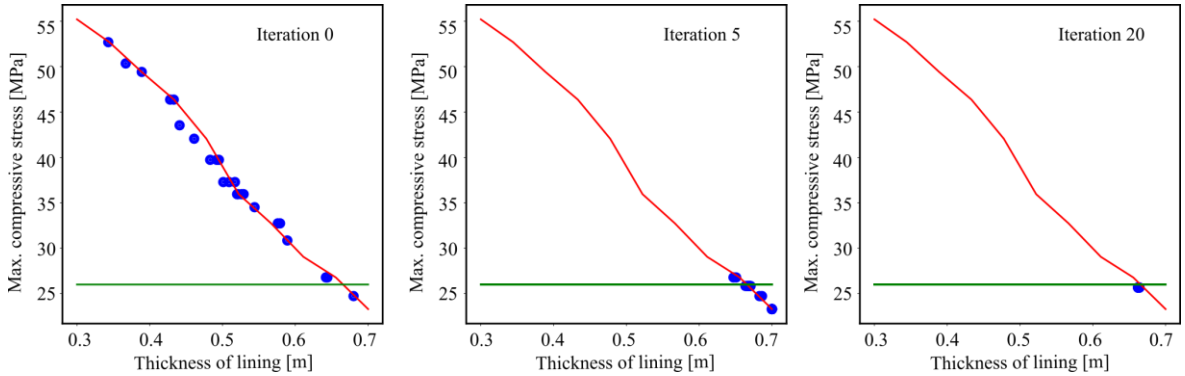

Fig. 11. Optimization of t_{lining} in a quasi-rectangular tunnel without the interior column.

5.2.2. With the interior column

Unlike the previous study, the current investigation incorporates t_{column} as an additional design variable, while the other parameters, i.e. H, E_s, and K_0, remain unchanged, including the PSO configuration. Two optimization scenarios are then investigated, taking into account the relative importance of t_{lining}, t_{column}, and σ_{max}, with t_{lining} being the top priority. In the first scenario, the objective is to minimize both t_{lining} and t_{column} while prioritizing σ_{max} as the second most important parameter (i.e. $t_{lining} > \sigma_{max} > t_{column}$). In the second scenario, t_{column} is given a higher priority than σ_{max} to achieve a more extreme optimization of the column thickness. To account for the order of importance during optimization, the PSO algorithm is modified to adjust the velocity update based on the importance index of each parameter, leading to superior convergence for the parameters with higher priorities.

Fig. 12 presents the PSO convergence for the first scenario, in which the green surface represents the stress limit (σ_{max} = 26 MPa). At iteration 0, all particles of the swarm are randomly generated with uniform distribution within the input space. From iteration 7 onwards, the particles begin to converge towards the optimal range for t_{lining} (0.3–0.5 m). It can be observed that at iteration 20, the particles gather around a specific value of t_{column} of approximately 0.5 m. The solution converges at iteration 38, where all particles localize at a final global solution of $t_{lining} \approx 0.38$ m and $t_{column} \approx 0.54$ m, corresponding to σ_{max} = 23.7 MPa.

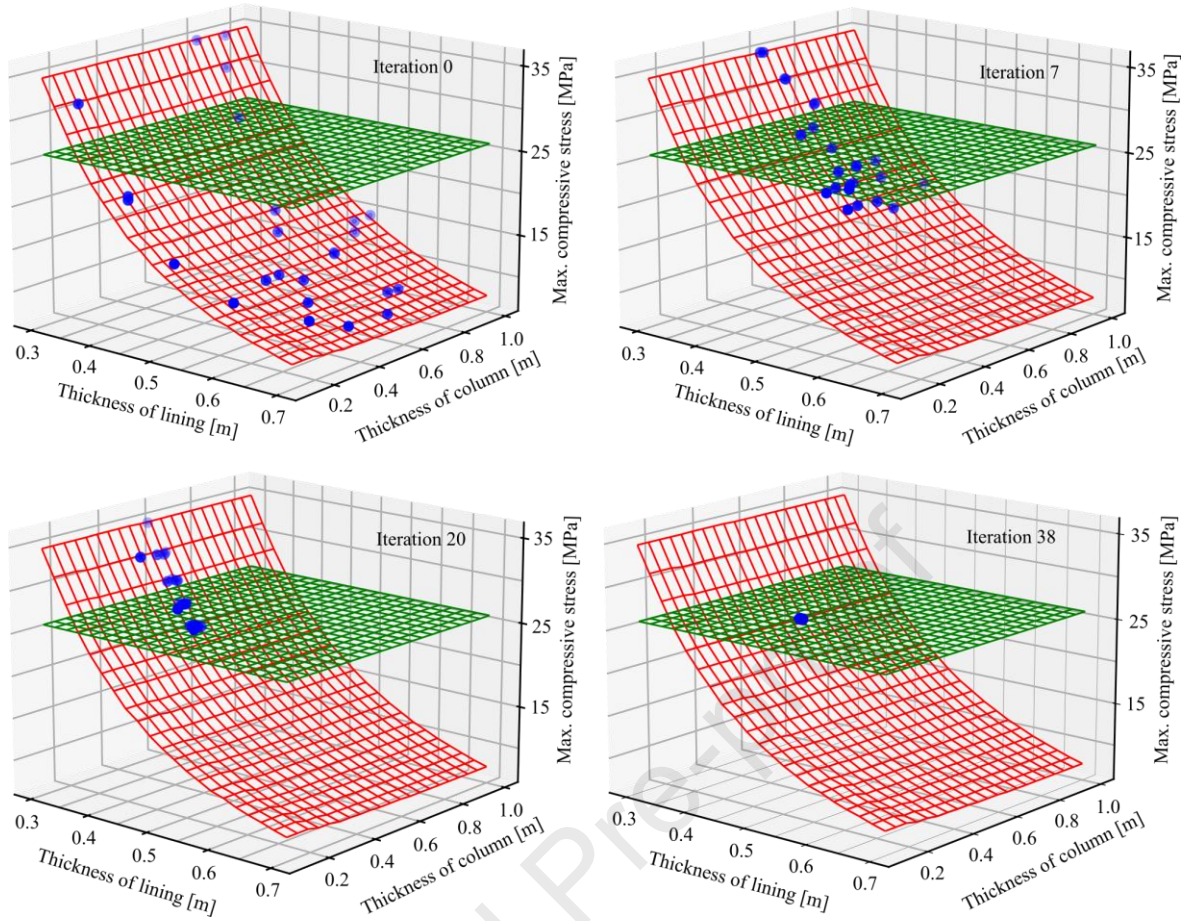

Fig. 12. Optimization of t_{lining} and t_{column} in a quasi-rectangular tunnel with an interior column (first scenario). Blue dots are particles on the response surface (in red).

In the second scenario, where t_{column} is given higher priority, it reaches a much smaller value without any reduction in the maximum stress, as illustrated in Fig. 13. In the initial stage, the particles of the swarm are randomly initialized, in a manner analogous to that observed in the previous scenario. Subsequently, in the later iterations, the particles are observed to move towards the optimal range for t_{lining} (0.3–0.5 m) and the lower bound for t_{column} = 0.1 m. The solution converges at iteration 20, with the optimal values of t_{lining} = 0.38 m and t_{column} = 0.1 m, corresponding to σ_{max} = 23.93 MPa. It is noteworthy that the PSO leads to an excessive optimization of the design variables, where t_{column} reaches its minimum value at the bound. However, the maximum stress remains below the limit. The difference in σ_{max} between the two scenarios is only 0.97%. This can be attributed to the fact that, given stress as the main priority, PSO will optimize the solution "at all cost" to meet the objective, resulting in the lowest possible stress but not necessarily the smallest t_{column}, which is a more crucial target when considering cost.

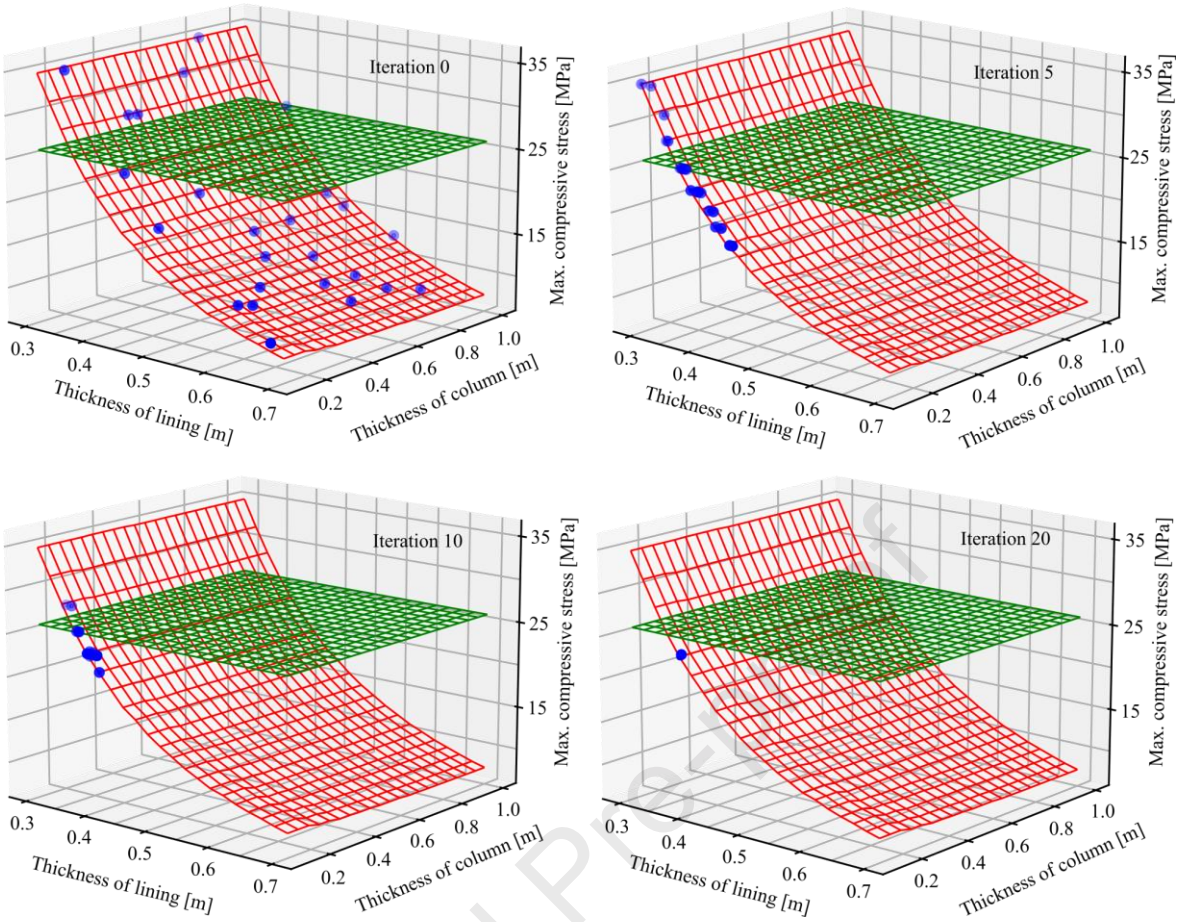

Fig. 13. Optimization of t_{lining} and t_{column} in a quasi-rectangular tunnel with an interior column (second scenario). Blue dots are particles on the response surface (in red).

The results obtained from the second scenario demonstrate that t_{column} can be significantly reduced without a substantial increase in critical stress. This, however, presents a better solution, given the relatively small difference in $\sigma_{\max}$ between the two cases. Both scenarios yield the same optimal value for t_{lining} = 0.38 m, which is 42% thinner than the optimal solution without an interior column. This further proves the positive impact of the interior column in enhancing the safety factor of the sub-rectangular tunnel.

The optimization results of all case studies are summarized in Table 10. It can be observed that, even at its optimal value, t_{column} has a minimal impact on the critical stress in the lining. Therefore, the thickness of the column should be determined based on other criteria, such as slenderness ratio or construction feasibility, rather than stress-based criteria.

Table 10. Optimized results of t_{lining} and t_{column} in three analyses.

Optimized scenario	Objective	t_{lining} (m)	t_{column} (m)	$\sigma_{\max}$ (MPa)
Without column	Minimum t_{lining}, $\sigma_{\max} \leq 26$ MPa	0.66	-	25.8
With column (first scenario)	Minimum t_{lining}, Minimum $\sigma_{\max}$ $\sigma_{\max} \leq 26$ MPa	0.38	0.54	23.7

With column (second scenario)	Minimum t_{lining}, minimum t_{column}, $\sigma_{max} \leq 26$ MPa	0.38	0.1	23.93

6. Conclusions

This work presents a novel HRM-XGBoost-PSO framework for the efficient design optimization of the quasi-rectangular tunnel which can be applied in real-time scenarios. The HRM method, originally developed for the analysis of conventional circular and rectangular tunnels, has been extended to accommodate quasi-rectangular tunnels with an interior column. This modeling approach was then validated against FEM concerning different shapes and dimensions. The results of the internal forces demonstrate that the interior column exerts a significant influence on the structural response of the tunnel.

Using the validated HRM model, different surrogate models were constructed employing widely used ensemble ML algorithms such as RF, GBDT, and XGBoost. The simulation dataset comprises five input parameters, two of which are the lining and interior column thickness. These surrogate models were then employed for stress prediction and for identifying the most important input factors affecting the structural response.

The feature important study shows that all five input parameters, namely E_s, H, K_0, t_{lining}, and t_{column}, are critical for accurately predicting both the maximum and minimum stresses in the lining. Furthermore, it is demonstrated that when the interior column is present, tunnel depth H is the most influential factor, whereas E_s is the dominant parameter when the interior column is not considered. In terms of efficiency, XGBoost outperforms other models, with an accuracy R^2 of 0.999 and a computation time of just a few seconds.

A multi-objective optimization is performed by combining the XGBoost model with the PSO algorithm to minimize maximum positive compressive stresses in the lining and to identify the optimal geometry for the quasi-rectangular tunnel, including the interior column as a binary parameter. The optimization results indicate that the interior column is necessary to achieve a balance between the cost objective, followed by the lining thickness, and the structural strength objective.

The utilization of multiple sophisticated and highly reliable algorithms in the study of input importance, generation of simulation datasets, and optimization of lining design serves to highlight the cutting-edge nature of this work. A direct comparison of the methods demonstrates that HRM-XGBoost-PSO is well-suited for the design optimization of quasi-rectangular tunnels. Although this study focuses on a specific tunnel case, we are confident that the framework

applies to other tunnel designs due to its high performance and accuracy. Furthermore, the influence of joints between segments in the lining and imperfect soil-lining interaction is not considered in the present study and will be the aim of future studies. Additionally, a user-friendly application interface is planned to facilitate the design process in tunnel engineering, allowing for the quick visualization of optimization results of the tunnel geometry concerning different design criteria.

Declaration of generative AI and AI-assisted technologies in the writing process

During the preparation of this work, the authors used ChatGPT to check spelling and grammar and improve the readability of the publication. After using this tool/service, the authors reviewed and edited the content as needed and took full responsibility for the content of the publication.

Acknowledgments

This research was funded by the Hanoi University of Mining and Geology (Grant No. T23-44). The research is also funded by the German Research Foundation (DFG – Project number 518862444) in collaboration with the Vietnam National Foundation for Science and Technology Development (NAFOSTED) under grant number DFG.105-2022.03. The third author was funded by the Postdoctoral Scholarship Program of the Vingroup Innovation Foundation (VINIF) (VINIF. 2023.STS.15). These supports are gratefully acknowledged.

References

Abdellah, W.R., Ali, M.A., Yang, H.S., 2018. Studying the effect of some parameters on the stability of shallow tunnels. J. Sustain. Min. 17, 20–33.

Blom, C., 2002. Design philosophy of concrete linings for tunnel in soft soils. PhD Thesis. Delft University of Technology, Delft, Netherlands.

Breiman, L., 2001. Random forests. Mach. Learn. 45, 5–32.

Bui, H., Cao, B.T., Freitag, S., Hackl, K., Meschke, G., 2023. Surrogate modeling for interactive tunnel track design using the cut finite element method. Eng. Comput. 39, 4025–4043.

Cao, B.T., Freitag, S., Meschke, G., 2016. A hybrid RNN-GPOD surrogate model for real-time settlement predictions in mechanised tunnelling. Adv. Model. Simul. Eng. Sci. 3, 1–22.

Cao, B.T., Obel, M., Freitag, S., Heußner, L., Meschke, G., Mark, P., 2022. Real-time risk assessment of tunneling-induced building damage considering polymorphic uncertainty. ASCE-ASME J. Risk Uncertain. Eng. Syst. Part A.–Civ. Eng. 8, 04021069.

Cao, B.T., Obel, M., Freitag, S., Mark, P., Meschke, G., 2020. Artificial neural network surrogate modelling for real-time predictions and control of building damage during mechanized tunnelling. Adv. Eng. Softw. 149, 102869.

Celik, S., 2017. Comparison of Mohr-Coulomb and hardening soil models numerical estimation of ground surface settlement caused by tunneling. J. Inst. Sci. Technol. 7 (4), 95–102.

Chen, K.H., Peng, F.L., 2018. An improved method to calculate the vertical earth pressure for deep shield tunnel in shanghai soil layers. Tunn. Undergr. Space Technol. 75, 43–66.

Chen, T., Guestrin, C., 2016. Xgboost: A scalable tree boosting system. In: Proceedings of the 22nd ACM SIGKDD International Conference on Knowledge Discovery and Data Mining. Association for Computing Machinery, New York, USA. p 785–794.

Dang, V.K., Do, N.A., Nguyen, T.T., Nguyen, A.D.H., Pham, V.V., 2021. An overview of research on metro tunnel lining in the sub-rectangular shape. J. Min. Earth Sci. 62, 68–78 (in Vietnamese).

Do, N.A., 2014. Numerical analyses of segmental tunnel lining under static and dynamic loads. PhD Thesis. INSA de Lyon, Lyon, France.

Do, N.A., Dias, D., 2018. Tunnel lining design in multi-layered grounds. Tunn. Undergr. Space Technol. 81, 103–111.

Do, N.A., Dias, D., Oreste, P., Djeran-Maigre, I., 2014. The behaviour of the segmental tunnel lining studied by the hyperstatic reaction method. Eur. J. Environ. Civ. Eng. 18 (4), 489–510..

Do, N.A., Dias, D., Zhang, Z., Huang, X., Nguyen, T.T., Pham, V.V., Nait-Rabah, O., 2020. Study on the behavior of squared and sub-rectangular tunnels using the hyperstatic reaction method. Transp. Geotech. 22, 100321.

Du, D., Dias, D., Do, N., 2018. Designing U-shaped tunnel linings in stratified soils using the hyperstatic reaction method. Eur. J. Environ. Civ. Eng. 24, 2422–2439.

Du, D., Dias, D., Do, N., 2020a. Effect of surcharge loading on horseshoe-shaped tunnels excavated in saturated soft rocks. J. Rock Mech. Geotech. Eng. 12, 1339–1346.

Du, D., Dias, D., Do, N., 2020b. Lining performance optimization of sub-rectangular tunnels using the hyperstatic reaction method. Comput. Geotech 117, 103279.

Du, D., Lei, D., Liu, K., Dias, D., 2022. Design of quasi-rectangular tunnel built in the rock masses following Hoek–Brown failure criterion. Buildings 12 (10), 1578.

Eberhart, R.C., Shi, Y., 2001. Particle swarm optimization: Developments, applications and resources. In: Proceedings of the 2001 Congress on Evolutionary Computation. IEEE,

Piscataway, USA. p. 81–86.

Elbaz, K., Yan, T., Zhou, A., Shen, S.L., 2022. Deep learning analysis for energy consumption of shield tunneling machine drive system. Tunn. Undergr. Space Technol. 123, 104405.

EN 1992-1-1:2004, 2004. Eurocode 2: Design of concrete structures – Part 1-1: General rules and rules for buildings. European Committee for Standardization, Brussels, Belgium.

Freitag, S., Cao, B.T., Niníc, J., Meschke, G., 2018. Recurrent neural networks and proper orthogonal decomposition with interval data for real-time predictions of mechanised tunnelling processes. Comput. Struct. 207, 258–273.

Friedman, J., 2001. Greedy function approximation: A gradient boosting machine. Ann. Stat. 29, 1189–1232.

Gong, C., Xie, C., Zhu, H., Ding, W., Song, J., Ge, Y., 2024. Time-varying compressive properties and constitutive model of EPDM rubber materials for tunnel gasketed joint. Constr. Build. Mater. 433, 136734.

Huang, H., Chang, J., Zhang, D., Zhang, J., Wu, H., Li, G., 2022. Machine learning-based automatic control of tunneling posture of shield machine. J. Rock Mech. Geotech. Eng. 14, 1153–1164.

Huang, X., Zhu, Y., Zhang, Z., Zhu, Y., Wang, S., Zhuang, Q., 2018. Mechanical behaviour of segmental lining of a sub-rectangular shield tunnel under self-weight. Tunn. Undergr. Space Technol. 74, 131–144.

ITA-WG2, 2019. Guidelines for the design of segmental tunnel linings. ITA Report n°22. International Tunnelling and Underground Space Association (ITA), Châtelaine, Switzerland.

Karasev, M., Nguyen, T., 2022. Method for predicting the stress state of the lining of underground structures of quasi-rectangular and arched forms. J. Min. Inst. 257, 807–821.

Kroetz, H.M., Do, N.A., Dias, D., Beck, A.T., 2018. Reliability of tunnel lining design using the hyperstatic reaction method. Tunn. Undergr. Space Technol. 77, 59–67.

Li, C., Wang, L., Li, J., Chen, Y., 2021b. Application of multi-algorithm ensemble methods in high-dimensional and small-sample data of geotechnical engineering: A case study of swelling pressure of expansive soils. J. Rock Mech. Geotech. Eng. 16, 1896–1917.

Li, F., Jiang, A., Zheng, S., 2021a. Anchoring parameters optimization of tunnel surrounding rock based on particle swarm optimization. Geotech. Geol. Eng. 39, 4533–4543.

Li, H., Chen, W., Tan, X., 2024. Estimation of tunnel axial orientation in the interlayered rock mass using a comprehensive algorithm. J. Rock Mech. Geotech. Eng. 16 (7), 2579–2590.

Li, P., Liu, X., Jiang, X., Zhang, X., Wu, J., Chen, P., 2023b. Investigation of the first quasi-rectangular metro tunnel constructed by the 0-θ method. Front. Struct. Civ. Eng. 17, 1707–1722.

Li, X., Zhao, S., Shen, Y., Li, G., Zhu, H., 2023a. Integrated parameter optimization approach: Just-

in-time (JIT) operational control strategy for TBM tunnelling. Tunn. Undergr. Space Technol. 135, 105040.

Liu, B., Wang, J., Wang, R., Wang, Y., Zhao, G., 2023. Intelligent decision-making method of tbm operating parameters based on multiple constraints and objective optimization. J. Rock Mech. Geotech. Eng. 15, 2842–2856.

Liu, X., Liu, Z., Ye, Y., Bai, Y., Zhu, Y., 2018b. Mechanical behavior of quasi-rectangular segmental tunnel linings: Further insights from full-scale ring tests. Tunn. Undergr. Space Technol. 79, 304–318.

Liu, X., Liu, Z., Yuan, Y., Zhu, Y., 2018a. Quasi-rectangular shield tunneling technology in the Ningbo rail transit project. In: Hordijk, D., Lukovíc, M. (Eds.), High Tech Concrete: Where Technology and Engineering Meet: Proceedings of the 2017 fib Symposium. Springer International Publishing, Cham, Switzerland. p. 2765–2773.

Liu, X., Ye, Y., Liu, Z., Huang, D., 2018c. Mechanical behavior of quasi-rectangular segmental tunnel linings: First results from full-scale ring tests. Tunn. Undergr. Space Technol. 71, 440–453.

Liu, Z., Chen, Y., Wu, Y., Liu, X., 2024. Experimental and theoretical investigations of the mechanical behavior of column-free quasi-rectangular segmental tunnel linings. Appl. Sci. 14, 2896.

Lundberg, S.M., Lee, S.I., 2017. A unified approach to interpreting model predictions. In: Proceedings of the 31st International Conference on Neural Information Processing Systems. Curran Associates Inc., Red Hook, USA. p. 4768–4777.

Miliziano, S., de Lillis, A., 2019. Predicted and observed settlements induced by the mechanized tunnel excavation of metro line C near S. Giovanni station in Rome. Tunn. Undergr. Space Technol. 86, 236–246.

Möller, S.C., 2006. Tunnel induced settlements and structural forces in linings. PhD Thesis. Stuttgart University, Stuttgart, Germany.

Nguyen, T.T., Do, N.A., 2024. Influence of interior column on the behaviour of quasi-rectangular tunnel. J. Min. Earth Sci. 65, 22–29.

Nguyen, T.T., Do, N.A., Anatolyevich, K.M., Dias, D., Dang, V.K., Aleksandrovna, V.M., 2022. Numerical investigation of the horseshoe tunnels structural behavior. Indian Geotech. J. 52, 799–814.

Oreste, P., 2007. A numerical approach to the hyperstatic reaction method for the dimensioning of tunnel supports. Tunn. Undergr. Space Technol. 22, 185–205.

Pham, V.V., Do, N.A., Dias, D., 2021. Sub-rectangular tunnel behavior under seismic loading. Appl.

Sci. 11, 9909.

Pham, V.V., Do, N.A., Dias, D., Nguyen, C.T., Dang, V.K., 2022. Sub-rectangular tunnel behaviour under static loading. Transp. Infrastruct. Geotechnol. 10, 488–503.

Plaxis, 2019. PLAXIS 2D reference manual. Bentley Systems International Limited, Dublin, Ireland.

Takano, Y.H., 2000. Guidelines for the design of shield tunnel lining. Tunn. Undergr. Space Technol. 15, 303–331.

Tang, L., Na, S., 2021. Comparison of machine learning methods for ground settlement prediction with different tunneling datasets. J. Rock Mech. Geotech. Eng. 13, 1274–1289.

Terzaghi, K., 1941. General wedge theory of earth pressure. Trans. Am. Soc. Civil Eng. 106, 68–80.

Tien, N.T., Anh, D.N., Anatolyevich, K.M., Van Kien, D., Daniel, D., 2020. Tunnel shape influence on the tunnel lining behavior. Proc. Inst. Civil Eng. – Geotech. Eng. 174, 355–371.

Timoshenko, S., 1976. Strength of materials, Part 1: Elementary theory and problems. Krieger Publishing Company, Malabar, USA.

Vinod, M., Khabbaz, H., 2019. Comparison of rectangular and circular bored twin tunnels in weak ground. Undergr. Space 4, 328–339.

Xu, C., Cao, B.T., Yuan, Y., Meschke, G., 2023. Transfer learning based physics-informed neural networks for solving inverse problems in engineering structures under different loading scenarios. Comput. Meth. Appl. Mech. Eng. 405, 115852.

Xu, C., Cao, B.T., Yuan, Y., Meschke, G., 2024. A multi-fidelity deep operator network (DeepONet) for fusing simulation and monitoring data: Application to real-time settlement prediction during tunnel construction. Eng. Appl. Artif. Intell. 133, 108156.

Yu, H., Chen, G., 2021. Pseudo-static simplified analytical solution for seismic response of deep tunnels with arbitrary cross-section shapes. Comput. Geotech. 137, 104306.

Zendaki, Y., Cao, B.T., Alsahly, A., Freitag, S., Meschke, G., 2024. A simulation-based soft-ware to support the real-time operational parameters selection of tunnel boring machines. Undergr. Space 14, 176–196.

Zhang, R., Li, Y., Goh, A.T., Zhang, W., Chen, Z., 2021. Analysis of ground surface settlement in anisotropic clays using extreme gradient boosting and random forest regression models. J. Rock Mech. Geotech. Eng. 13, 1478–1484.

Zhang, W., 2021. Numerical and experimental analysis of the mechanical behaviour of linings in quasi-rectangular shield tunnels. PhD. Thesis. Ghent University, Ghent, Belgium.

Zhang, W., De Corte, W., Liu, X., Taerwe, L., 2020. Influence of rotational stiffness modeling on the

joint behavior of quasi-rectangular shield tunnel linings. Appl. Sci. 10, 8396.

Zhang, W., De Corte, W., Liu, X., Taerwe, L., 2022a. A comparative investigation between the beam spring method and the modified routine method in special-section shield tunnels: A case study for quasi-rectangular tunnels. Int. J. Numer. Anal. Methods Geomech. 46, 1754–1781.

Zhang, W., Liu, X., Liu, Z., Zhu, Y., Huang, Y., Taerwe, L., De Corte, W., 2022b. Investigation of the pressure distributions around quasi-rectangular shield tunnels in soft soils with a shallow overburden: A field study. Tunn. Undergr. Space Technol. 130, 104742.

Zhang, Z., Zhu, Y., Huang, X., Zhu, Y., Liu, W., 2019. 'Standing' full-scale loading tests on the mechanical behavior of a special-shape shield lining under shallowly-buried conditions. Tunn. Undergr. Space Technol. 86, 34–50.

Zhao, C., Chen, L., Ni, P., Xia, W., Wang, B., 2024. A modified back analysis method for deep excavation with multi-objective optimization procedure. J. Rock Mech. Geotech. Eng. 16, 1373–1387.

Zhao, M., Li, H., Huang, J., Du, X., Wang, J., Yu, H., 2021. Analytical solutions considering tangential contact conditions for circular lined tunnels under longitudinally propagating shear waves. Comput. Geotech. 137, 104301.

Zhu, Y., Zhang, Z., Huang, X., Zhu, Y., 2018. Numerical investigation on the mechanical characteristics of a special-shaped shield lining with a large cross-section. In: Zhang, D., Huang, X. (Eds.), Proceedings of GeoShanghai 2018 International Conference: Tunnelling and Underground Construction. Springer Singapore, Singapore. p. 384–391.

Dr. Ba Trung Cao is the leader of two research groups at the Institute for Structural Mechanics, Ruhr University Bochum (RUB), Germany, namely "Computational Intelligence and Structural Reliability" and "Computational Modeling in Tunneling and Underground Structures". He received his PhD degree from RUB in 2018, having focused his studies on computational tunnel engineering. His research interests include computational models and digitalization in tunnel and underground engineering, the application of machine learning and computational intelligence in civil engineering, the physics-informed machine learning in applied mechanics, and the uncertainty quantification in structural mechanics.

Declaration of interests

☒ The authors declare that they have no known competing financial interests or personal relationships that could have appeared to influence the work reported in this paper.

☐The authors declare the following financial interests/personal relationships which may be considered as potential competing interests: